https://doi.org/10.5194/egusphere-2026-2722
Preprint. Discussion started: 21 September 2026

Feasibility study of atmospheric carbon dioxide satellite retrievals over snow in the context of the Copernicus Anthropogenic CO_2 Monitoring Mission

Amanita Mikkonen[1,2,*], Hartmut Bösch[2], Jouni Peltoniemi[3], Leif Vogel[4], Antonio Di Noia[5], Ella Kivimäki[1], Miia Salminen[1], Maria Gritsevich[3], Yasjka Meijer[6], and Hannakaisa Lindqvist[7,*]

[1]Space and Earth Observation Centre, Finnish Meteorological Institute, Erik Palménin aukio 1, FI-00101 Helsinki, Finland
[2]Institute of Environmental Physics, University of Bremen, D-28334 Bremen, Germany
[3]Finnish Geospatial Research Institute FGI of the National Land Survey of Finland, Vuorimiehentie 5, 02150 Espoo, Finland
[4]Kaioa Analytics, Mundaka, Spain
[5]Department of Civil and Computer Engineering, Tor Vergata University, Via del Politecnico 1, 00133 Rome, Italy
[6]European Space Agency (ESA), Keplerlaan 1, 2201 AZ Noordwijk, The Netherlands
[7]Space and Earth Observation Centre, Finnish Meteorological Institute, Tähteläntie 62, FI-99600 Sodankylä, Finland
[*]These authors contributed equally to this work.

Correspondence: Amanita Mikkonen (amanita.mikkonen@fmi.fi), Hannakaisa Lindqvist (hannakaisa.lindqvist@fmi.fi)

Abstract.

Northern high latitudes pose significant challenges to reliable space-based observations of total column carbon dioxide (XCO_2). In addition to large solar zenith angles and frequent cloud coverage over the Arctic and boreal regions, snow-covered surfaces absorb strongly in the shortwave-infrared wavelengths coinciding with the CO_2 absorption channels used by several current missions, e.g., Japanese Greenhouse Gases Observing Satellite and Nasa Orbiting Carbon Observatory-2, and the upcoming Copernicus Anthropogenic CO_2 Monitoring Mission (CO2M). Because of the resulting low radiances of the reflection measured by the satellite instruments, retrievals over snow may be less reliable and, for current missions, are typically filtered or flagged for potentially poor quality. In this work, we present the first feasibility study dedicated to XCO_2 retrievals over snow. We introduce a measurement-based snow reflectance model, develop this into a kernel format following the Ross-Thick-Snow (RTS) kernel formulation, and use this to simulate CO2M radiances. Furthermore, we also present a sample of simulated XCO_2 retrievals for the CO2M with the University of Leicester Full Physics (UoL-FP) retrieval framework, considering a variety of solar zenith angles as well as nadir and specular reflection (glint) observing geometries, the two planned observation modes of CO2M. The results indicate the advantages of using a snow kernel model in the retrievals of XCO_2, in terms of improved convergence. Glint-mode observations are shown to lead to higher signal-to-noise ratios and improved retrievals in terms of reduced errors compared to the nadir geometry in the Northern high latitudes over snow. The signal-to-noise ratio increases towards forward-scattering direction, which indicates that the exact specular reflection (glint) geometry is not required but forward scattering directions in general have advantages at large solar zenith angles. However, we also find that constraining the snow reflectance model is essential for the retrieval improvements. The results show the potential to significantly increase the number of observations at high latitudes and widen the seasonal coverage by approximately 1-3 months. The relevance of

https://doi.org/10.5194/egusphere-2026-2722
Preprint. Discussion started: 21 September 2026

a potentially increased coverage does not limit to CO2M but extends to other current and future CO_2 missions as well as other atmospheric constituents. Ultimately, the increased coverage may contribute to the quantification and an improved understanding of high-latitude CO_2 sources and sinks, especially in the late winter and spring seasons where a reliable quantification of the XCO_2 seasonal cycle is essential.

1 Introduction

Space-based observations of carbon dioxide (CO_2) have recently reshaped our understanding of the global carbon cycle. Near-global CO_2 observations from the Greenhouse Gases Observing Satellite (GOSAT; Yokota et al. 2009), Orbiting Carbon Observatory -2 (OCO-2; Crisp et al. 2004), and TanSat (Yang et al., 2018) have revealed the value of satellite observations in increasing our knowledge on the carbon cycle by adding coverage to previously understudied and remote regions, such as the tropical oceans (Chatterjee et al., 2017), and tropical Africa (Palmer et al., 2019). These observations have also been utilized for an evaluation of country-level CO_2 emissions (Byrne et al., 2023) which demonstrates the relevance of these observations for supporting policymaking. The preparations for the Copernicus Anthropogenic CO_2 Monitoring Mission (CO2M) drive the development of these observations towards the detection of anthropogenic emissions with the goal of monitoring and verifying national carbon emission reductions (Janssens-Maenhout et al., 2020; Meijer et al., 2023).

Vast understudied regions with uncertainties in both natural and anthropogenic CO_2 fluxes remain in the Arctic and boreal zones. The carbon cycle at Northern high latitudes is currently under rapidly changing conditions due to Arctic amplification (Rantanen et al., 2022), changing cryosphere (Pulliainen et al., 2020), and resulting potential feedback mechanisms. Particularly notable recent in situ measurement-based analyses of the changing carbon cycle include the enhancement of the boreal springtime carbon uptake (Pulliainen et al., 2017) and acceleration of seasonal carbon uptake and respiration in the Arctic (Jeong et al., 2018). Satellite observations have revealed an enhanced autumn respiration (Byrne et al., 2022), and multi-decadal proxies suggest a strong interannual variability in carbon uptake and respiration (Pulliainen et al., 2024). The increased accessibility of the Arctic also increases human activity (Meier et al., 2014) in terms of energy production, transport, oil and gas industry, and increasing natural gas production which may collectively lead to enhanced anthropogenic emissions. Reliable satellite observations of greenhouse gases are therefore necessary for the quantification of these emissions and the evolution of natural processes through the Arctic and boreal regions.

Northern high latitudes pose numerous challenges to satellite instruments that measure reflected and scattered solar radiation in the near- and shortwave infrared wavelengths (NIR and SWIR) for retrievals of CO_2. The main limiting factor for these observations is the lack of solar radiation during the polar night and, for most seasons, large solar zenith angles (SZA) that lead to a large airmass for the signal, meaning an enhanced impact of atmospheric scattering that complicates the interpretation of the path length of radiation. Another challenge is seasonally or permanently snow-covered surfaces. Snow reflectance is strongly wavelength-dependent, driven by the dielectric properties of ice (see, e.g., Warren and Brandt, 2008; Lindqvist et al., 2018): while snow appears white and highly reflective in the visible wavelengths, it becomes strongly absorbing in the near-infrared wavelengths (Peltoniemi et al., 2005, 2009; Hannula et al., 2020), hampering especially the signal in the CO_2 absorption band

https://doi.org/10.5194/egusphere-2026-2722
Preprint. Discussion started: 21 September 2026

around 2.0 μm, often referred to as the strong CO_2 band or, in the context of CO2M, the SWIR-2 channel (Mikkonen et al., 2024). Large SZA and low signal-to-noise ratio (SNR) increase the possibility for large biases in the retrieved column-averaged dry air mole fraction of CO_2 (XCO_2); therefore, observations over snow are largely filtered (O'Dell et al., 2018), resulting in a limited seasonal coverage of high-latitude XCO_2 retrievals (Lindqvist et al., 2015; Jacobs et al., 2020). Recently, high-latitude XCO_2 retrievals from OCO-2 have been improved by introducing a more accurate digital elevation model for high latitudes (Jacobs et al., 2023).

Despite recent advances for existing missions, there may still be potential to increase the observational coverage of high latitudes for the future CO2M observations by investigating the feasibility of CO_2 retrievals over snow. Mikkonen et al. (2024) have shown that accounting for a realistic bi-directional reflectance distribution function (BRDF) of snow, the reflected radiances can be larger towards forward-scattering directions over snow. This suggests that the potential of making CO_2 retrievals over snow should be evaluated, accounting for a realistic snow surface model and testing with different observational geometries. CO2M will have two observation modes: directly downward viewing nadir mode, which is the primary observation geometry over land, and towards the direct specular reflection viewing glint mode, which has been initially intended to make observations over water, but it could improve observations over snow-covered land as well. In this work, we revisit the snow BRDF modelling and employ kernel-based models to be tested to explore the feasibility of making retrievals of XCO_2 over snow-covered surfaces. Our focus and motivation is improving the high-latitude coverage for the future CO2M observations; therefore, this study uses only simulated observations. We will also motivate the need for addressing snow-covered surfaces by showcasing seasonal snow extent over high-latitude regions. In Sect. 2, we introduce the snow reflectance measurement data set used to inform the snow BRDF model and satellite-based snow coverage data for the regional analysis. Section 3 introduces the methods for snow reflectance modelling, statistical snow coverage analysis, radiative transfer modelling, and XCO_2 retrieval setup. In Sect. 4, the results are shown, and discussed in Sect. 5. Conclusions and their applicability to existing missions are presented in Sect. 6.

2 Data description

2.1 Snow reflectance measurements

Finnish Geospatial Research Institute (FGI) hosts a database of snow reflectance measurements collected over 20 years of in-situ measurements with a field goniospectrometer (FIGIFIGO; Peltoniemi et al. 2015, 2010). From the snow measurements database, three snow types were selected for further analyses: new snow, hard snow, and old snow. The criteria for the selection were the representativeness and quality of these cases. Considering that the potential improvements in coverage for CO_2 retrievals would realistically aim for late winter or spring months in the high latitudes, the old snow type which represents a snow surface that has aged for a minimum of several days after snowfall and has typically a larger grain size, is likely the most representative seasonal snow surface for late winter and early spring conditions. Hard snow is dense, wind-packed snow, which is found primarily on glaciers, and new snow represents fresh snowfall. Inclusion of several different snow types is important for understanding and simulating natural variability. The reflectance model based on these data is described in Sect. 3.1.

https://doi.org/10.5194/egusphere-2026-2722
Preprint. Discussion started: 21 September 2026

2.2 Snow coverage data

The snow coverage data used in this study is based on the GlobSnow v3.0 Snow Water Equivalent (SWE) product (Pulliainen et al., 2020; Luojus et al., 2021), supplemented with snow clearance day data (Takala et al., 2009). Both datasets are based on microwave satellite observations. This combination of datasets was employed to provide a daily snow cover estimate, as the GlobSnow SWE dataset does not include observations for every day. Furthermore, since the snowmelt period can be relatively long, the GlobSnow dataset was also used to determine whether a given pixel is partially snow-covered for a given day during the spring-melt period. In the GlobSnow SWE product, satellite-based microwave observations are combined with ground-based snow depth measurements to estimate SWE, while the snow clearance day data is a separate product that defines the snowmelt timing in spring for each pixel individually based on satellite observations.

The snow coverage data are in the EaseGrid-1 projection format, with a spatial resolution of 25 km × 25 km (Fig. 1). The dataset contains daily information for each grid cell regarding the snow cover state, with possible classifications being snow-free landscape, patchy snow cover and full snow cover. The snow data were produced for December, January, February, March, April, and May from 2012 to 2018. The analysis methods for these data are presented in Sect. 3.2 and the results in Sect. 4.1.

3 Methods

3.1 Snow reflectance modelling

To model the snow surface reflectance based on the measurements described in Section 2.1, two strategies were first considered: Legendre polynomial fitting and kernel models. A Legendre polynomial fit was found to work best for the interpolation range, and kernel models for extrapolation, e.g., for multiple-scattering computations or in cases of strong surface roughness causing shadows. Due to the angular sparsity of the measurement data and high dimensionality of a BRDF, the kernel approach was selected for further use in the present study.

The RTS kernel model by Ding et al. (2019) was adopted. This model replaces the geometric term in the traditional RossThick-Roujean (RTR) model by Roujean et al. (1992) with a snow kernel, K_{snow}, and thus fits more realistically the forward-increasing enhancement seen in the measurements. The modified model fully written out is

$$R(\theta_{\mathrm{s}},\theta_{\mathrm{v}},\phi,\lambda) = f_{\mathrm{iso}}(\lambda) + f_{\mathrm{vol}}(\lambda)K_{\mathrm{vol}}(\theta_{\mathrm{s}},\theta_{\mathrm{v}},\phi) + f_{\mathrm{snow}}(\lambda)K_{\mathrm{snow}}(\theta_{\mathrm{s}},\theta_{\mathrm{v}},\phi), \quad (1)$$

where θ_s and θ_v are the solar and viewing zenith angles, ϕ is the azimuth angle difference between the solar and viewing directions, λ is the wavelength of the reflected radiation, f_{iso}, f_{vol} and f_{snow} are the wavelength-dependent isometric, volumetric and, snow coefficients, respectively, and K_{vol} and K_{snow} are the volumetric and snow kernels:

$$K_{\mathrm{vol}} = \frac{\left(\frac{\pi}{2} - \xi\right)\cos\xi + \sin\xi}{\cos\theta_s + \cos\theta_v} - \frac{\pi}{4} \quad (2)$$

and

$$K_{\mathrm{snow}} = \left(\frac{C_1 + C_2(\cos\theta_s + \cos\theta_v) + C_3\cos\theta_s\cos\theta_v + P(\xi)}{4(\cos\theta_s + \theta_v)}\right)(1 - \alpha\cos\xi\exp(-\cos\xi)) + 0.4076\alpha - 1.1081, \quad (3)$$

https://doi.org/10.5194/egusphere-2026-2722
Preprint. Discussion started: 21 September 2026

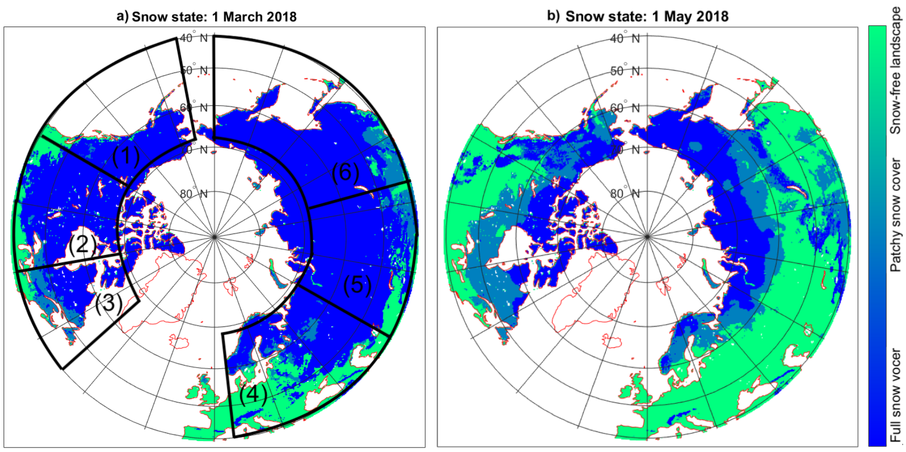

Figure 1. Snow cover state on (a) 1 March 2018 and (b) 1 May 2018. The borders of the six case study areas used for the snow cover analysis are outlined in black in (a). The areas are numbered starting from the westernmost case study area.

where

$$P(\xi) = 11.1e^{-0.087(180-\xi(180/\pi))} + 1.1e^{-0.014(180-\xi(180/\pi))}. \tag{4}$$

The parameters C_1, C_2, C_3, and α are 1.247, 1.186, 5.157, and 0.3, respectively. The angle ξ is the scattering angle, which as a function of zenith and azimuth angles is

$$\xi = \arccos\left(\cos\theta_s \cos\theta_v + \sin\theta_s \sin\theta_v \cos\phi\right). \tag{5}$$

For limited range of data, the kernel model provides a safer fit than polynomials because it remains smooth even in hard extrapolations where polynomial fits may diverge unpredictably. To better consider ground pixels mixed with vegetation, trees, or considerable snow surface roughness, adding the geometric kernel of the RTR model could be beneficial, but that was out of scope of this study.

The presented approach extends and robustifies the snow BRDFs presented by Mikkonen et al. (2024). The kernel model is suitable when extrapolation to a full hemisphere is needed, e.g., in multiple scattering computations and retrieval algorithms, and the polynomial fit for single-scattering calculations, or when the surface is rough enough to cast significant shadows. For consistency, in the present work the kernel model is used in all radiative transfer simulations (Sect. 3.3 and 4.3) and retrieval studies (Sect. 3.4 and 4.4).

3.2 Average regional snow coverage

To showcase the geographical distribution of snow coverage we divided land regions between 40° N–68° N to six case study areas (Fig. 1 (a)). Each case study area was further subdivided into 14 latitude zones, each being two degrees wide in longitude. The three North American case study areas included longitude ranges 50° W–80° W, 80° W–120° W and 120° W–170° W. The

https://doi.org/10.5194/egusphere-2026-2722
Preprint. Discussion started: 21 September 2026

three Eurasian areas were located within longitude ranges 5° E–60° E, 60° E–105° E and 105° E–180° E. For each latitude zone of all case study areas, we calculated the daily mean snow coverage for the period 2012–2018 and the standard deviation from the mean value. Thus, statistics on the temporal evolution of regional snow cover were obtained. Case study areas with varying latitude zones were selected to represent different categories of climate and snow conditions, to capture the varying hemispheric snow cover patterns and spring recovery dynamics (Pulliainen et al., 2020).

3.3 Radiative transfer simulations

In Sect. 4.3 we apply two different radiative transfer (RT) codes hosted and developed at FMI for the simulations: 1) a fast RT code Raysca and 2) a backward Monte Carlo RT code Siro. The main difference between the codes is that Siro is able to simulate arbitrarily many orders of scattering whereas Raysca is limited only to the first order of scattering. Both codes can process identical input of atmospheric constituents and their spectroscopy. Both Raysca and Siro are publicly available as part of the ARSCA software package (`https://github.com/amikko/arsca`) which may be used freely in accordance to the MIT License.

Siro is a well-established, thoroughly validated backward Monte Carlo RT simulator initially created for studying multiple-scattered solar radiation in limb-viewing geometries. Its capabilities include the simulation of polarized radiation in a fully 3D atmosphere with varying surface albedo (Oikarinen et al., 1999; Oikarinen, 2001, 2002). Recently, Siro has been used as a validation model in RT model development (Mikkonen et al., 2024, 2025) and when compared to other RT models, Siro agreed within computational precision in single-scattering and $2-4\%$ in multiple scattering simulations (Zawada et al., 2021).

Raysca is a newer RT code, which simulates the propagation of polarized light in arbitrary media and geometries in the NIR-SWIR wavelength regions (Mikkonen et al., 2024). It is limited to single-scattering simulations, which is a fair approximation of atmospheric radiative transfer in a clear-sky case in the NIR-SWIR wavelengths.

3.3.1 Radiative transfer model inputs

The atmosphere in the simulations considers Rayleigh scattering and it has standard vertically varying distributions of CO_2, H_2O, O_2, CH_4, O_2-O_2, NO_2 and O_3, whose absorption spectra are obtained and calculated using the HITRAN API (Kochanov et al., 2016). Siro is used in the simulations where multiple scattering is essential, i.e., for test cases with increased atmospheric scattering by optically thin clouds.

Atmospheric composition and conditions for the simulations were adapted from the prior information in the GGG2020 retrieval process for the Total Carbon Column Observing Network observations over Sodankylä, Finland on April 21st 2020 (Kivi et al., 2022). This is a representative atmosphere of usual spring conditions in the northern latitudes. The GGG2020 contained the vertical concentrations of the considered absorbing gases and the temperature, pressure and number density profiles necessary for absorption cross-section computations.

For the three main bands in the CO2M framework (Meijer et al., 2023) for CO_2 retrievals (NIR, SWIR-1, SWIR-2), a number of discrete wavelengths were simulated with the absorption cross-sections computed at 0.02 cm^{-1} resolution: in the NIR band (747 – 773 nm) 22516 wavelengths, in the SWIR-1 band (1590 – 1675 nm) 15960 wavelengths, and in the SWIR-2 band (1990

https://doi.org/10.5194/egusphere-2026-2722
Preprint. Discussion started: 21 September 2026

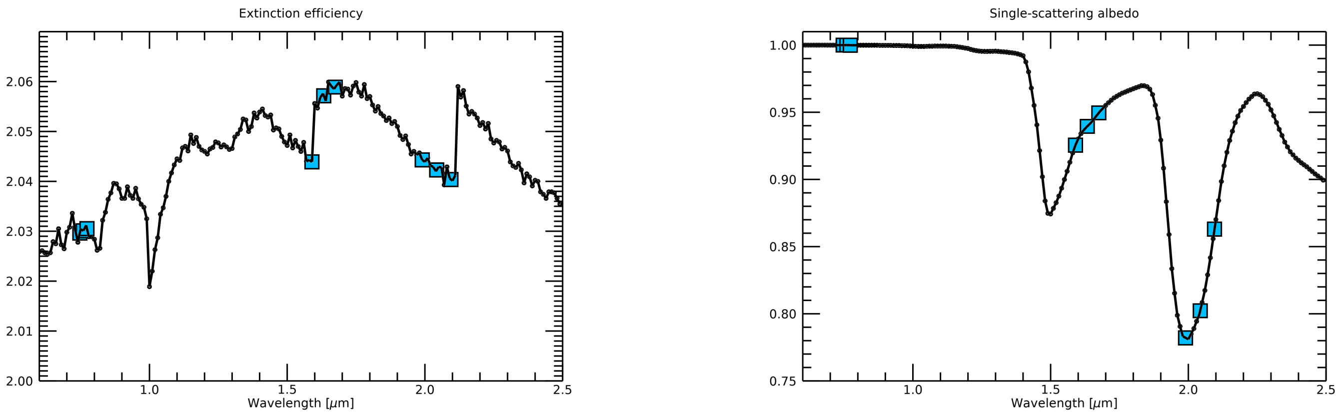

Figure 2. The extinction efficiency and single-scattering albedo of the ice crystals at different wavelengths. The NIR, SWIR-1, and SWIR-2 bands' lower and upper wavelength boundaries and the mid-band wavelength are highlighted with the blue squares.

– 2095 nm) 12595 wavelengths. The simulated spectra were convolved using a Gaussian slit with CO2M wavelength resolution for each of the bands. The convolved spectra were then interpolated onto evenly spaced CO2M wavelength channels, with 217, 283, and 300 discrete wavelengths for NIR, SWIR-1 and SWIR-2, respectively.

Solar zenith angles of 55, 60, 65 and 70 degrees, which represent commonly encountered illumination conditions in high latitudes during the shoulder seasons, were examined. CO2M is expected to produce XCO_2 retrievals at all SZA < 70 degrees. The satellite viewing geometry was obtained from Sentinel-7 (CO2M) Orbit Simulator. The satellite altitude was 793 km and the viewing angle of the swath was 9 degrees. A representative solar azimuth angle of 1 degree was identified in the >45 degrees latitude region and it was used in all of the radiance simulations.

In the Raysca RT model, a step size of 0.7 km was used for computing the radiation propagating along each viewing direction and a step size of 1.5 km was used for contributing beams of single-scattered radiation. A beam of radiation was simulated until its transmissivity was reduced below 10^{-10} or it exited the atmospheric medium.

Using the multiple scattering RT model Siro, we tested the effect of optically thin cirrus clouds on the radiance levels. Due to the increased computation time of Siro compared to Raysca, only the centre pixel of the viewing swath was simulated. We do not address cloud filtering here but assume that scenes with optically thick clouds would be identified by the cloud filtering procedures (as shown for existing missions, e.g., by Taylor et al. (2016)). The more problematic ones for the CO_2 retrievals are optically thin clouds that may pass the cloud screening. Particularly relevant for the high Northern latitudes are optically thin cirrus clouds composed of ice crystals and situated above snow surfaces. We address this with few test cases that include a uniform layer of optically thin cirrus at a varying altitude in snow surface conditions.

The ice cloud was chosen to have a cloud optical depth of 0.05, which is difficult to detect, but still causes considerable scattering. Two Gaussian cloud profiles were considered: at 0.75 km and at 6 km altitudes. The altitudinal standard deviation of the cloud was 0.25 km and it was uniform in latitudinal and longitudinal directions. The ice crystals were both absorbing and scattering, and their spectral extinction efficiency and single-scattering albedo are presented in Fig. 2.

https://doi.org/10.5194/egusphere-2026-2722
Preprint. Discussion started: 21 September 2026

The wavelength-dependent Müller matrices, extinction efficiencies and single-scattering albedos of ice crystals were based on a pre-computed database of randomly oriented ice crystals by Yang et al. (2013) and Baum et al. (2014). More specifically, the matrices are titled *Severely roughened hexagonal column ice crystal aggregates* from the MODIS6 collection and their effective diameter is 70 micrometers.

3.4 Retrieval of XCO_2 with the UoL-FP framework

The UoL-FP algorithm has been developed to retrieve XCO_2 from a simultaneous multi-band fit to the NIR, SWIR-1 and SWIR-2 wavelength bands. The main components of the algorithm are the forward model and the inverse method. The inverse scheme employs an iterative scheme based on Bayesian optimal estimation to determine a state vector x that includes a set of atmospheric, surface, and instrument-related parameters. The forward model describes the physics of the measurement process and models the top-of-the-atmosphere (TOA) radiance spectrum for a given geophysical state. The forward model of UoL-FP includes a radiative transfer solver which combines three different radiative transfer models (RTMs) coupled to a model of the solar spectrum to calculate the monochromatic spectrum of light that originates from the Sun that then passes through the atmosphere, reflects from the Earth‘s surface or scatters back from the atmosphere, and exits at the top of the atmosphere and enters an instrument. This TOA radiance spectrum is subsequently passed through the instrument model to simulate the measured radiances at the spectral resolution of the instrument.

The three RTMs used in UoL-FP are

- LIDORT: a full multiple-scattering RTM that solves the radiative transfer equation to high accuracy at a high number of streams (Spurr, 2004)
- TWOSTREAM: a fast two-stream multiple-scattering code (Spurr and Natraj, 2011)
- 2OS: a fast single-scattering radiative transfer model (Natraj et al., 2008)

The three RTMs are implemented to save computational time via the low stream interpolation (LSI) scheme (O’Dell, 2010). All of the RTMs are linearized so that analytical Jacobians, i.e. derivatives of the top of atmosphere radiance with respect to the different state vector elements, can be computed. The RTS BRDF model described in Sect. 3.1 has here been implemented in all three RTMs used in UoL-FP. A more detailed description of UoL-FP can be found in Boesch et al. (2011) and Cogan et al. (2012).

3.4.1 Model inputs and setup of retrieval experiments

The UoL-FP retrieval algorithm was used to simulate CO2M spectra over snow for a range of scenarios. This includes the three different snow types, aerosol optical depths ranging from 0.05 to 0.2, solar zenith angles ranging from 50° to 80°, for atmospheric profiles for two different locations in March and October for nadir and glint geometry. The parameters for the simulations are summarised in Table 1.

https://doi.org/10.5194/egusphere-2026-2722
Preprint. Discussion started: 21 September 2026

Parameter	Values
Atmospheric Profiles	CAMS model data (CO_2 , CH_4, H_2O, T) for 2 locations (Finland and Siberia) for March and October
Aerosols	AOD = [0.05, 0.1, 0.15, 0.2]
	Gaussian-shaped profile centred at 850hPa with 50hPa width
	Sulfate (Siberia) or seasalt (Finland) aerosol type
Surface BRDF	Hard snow, old snow, new snow
Geometry	SZA = [50° , 60° , 65° , 70° , 75°, 80°]
	Nadir (viewing zenith angle = 0°)
	Glint (viewing zenith angle = SZA)

Table 1. Baseline parameters for all simulations using UoL-FP. These parameters were varied according to the respective experiment.

We have carried out two different retrieval experiments. In the first experiment, we have perturbed the CO_2 profile by adding a 10 ppm CO_2 enhancement to the lowest 4 levels of the a priori CO_2 profile roughly representing the boundary layer. All other parameters including the surface BRDF are identical to the simulations. In the second experiment, we have retrieved simulated spectra computed with the old snow BRDF by using the new snow or hard snow BRDF in the retrieval. All atmospheric a priori assumptions are as in the simulations.

The retrieval of the simulated spectra includes a 20-level CO_2 profile, multiplicative scaling factors for the H_2O and CH_4 profile, an additive factor for the temperature profile, mean pressure height and total AOD of an aerosol profile for a single aerosol type and the first kernel parameter (f_{iso}) of the RTS BRDF for each band.

4 Results

4.1 Geographical and temporal distribution of snow coverage

We studied the geographical and temporal distribution of snow coverage on six case study areas (Fig. 1) in North America and Eurasia. Figure 3 shows, as an example, the mean snow fraction for the central North American study area (Area 2 in Fig. 1(a)) and the easternmost Eurasian study area (Area 4 in Fig. 1(a)), calculated as an average over the years 2012–2018. Similar figures for the remaining four case study areas are shown in Appendix, Fig. A1.

Figures 3 and A1 show that there are large differences in the seasonal snow fraction not only between the case study areas but also within the same latitude bands, driven by differences in the geography and topography. For example, when comparing the snow fraction time series from Areas 2 and 4 in Fig. 3, the differences between similar latitudes are notable, mainly because Area 2 is located in central Canada, whereas Area 4 is situated in Eastern Europe, close to the Atlantic Ocean. Therefore, they partly represent different climatic conditions. Generally, the figures show that in the southernmost latitude zone (40–42°N), the snow cover during winter can be patchy, with the snow cover fraction remaining clearly below 0.5 throughout the winter season. Snow also tends to melt before the end of March at the southernmost latitudes. In contrast, in the northernmost latitude zone (66–68°N), snow fraction can remain close to 0.5 even in the end of May, and total snow melt will take place in June.

https://doi.org/10.5194/egusphere-2026-2722
Preprint. Discussion started: 21 September 2026

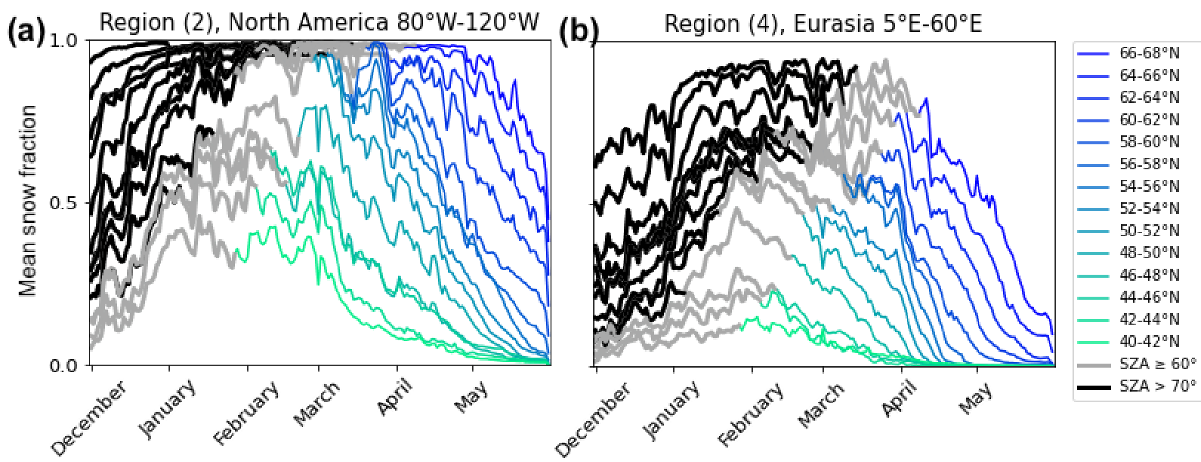

Figure 3. Mean snow fraction for (a) the central North American study area (Area 2 in Fig. 1) and (b) the easternmost Eurasian study area (Area 4 in Fig. 1) averaged over the years 2012—2018. Each line represents a two-degree latitude zone, and the lines are coloured according to the latitude zones. Gray and black lines in the latitude zones denote periods when SZA exceeds 60° and 70°, respectively, at 11:30 local time.

In winter and shoulder seasons, satellite observations are hampered by large solar zenith angles in addition to snow surfaces. To demonstrate the co-existence of snow cover together with large SZA during the CO2M overpass at 11:30 local time, Figs. 3 and A1 show the SZA range of 60°–70° with gray color and SZA > 70° (when CO2M retrievals may become too challenging) with black. Based on the figures, it can be stated that a high solar zenith angle (i.e., SZA > 70°) is not a limiting factor for retrievals over latitudes 40–46°N, where in all case study regions at least patchy snow cover exists during winter. For the northernmost latitude zones (62–68°N), SZA remains large until the first half of March, but the snow fraction at those latitude zones can deviate from zero until June, indicating that there can be two to three months in spring when snow cover is significant and the solar zenith angle is less than 70°. The length of the time period when the SZA is between 60°–70° depends on the latitude zone and varies approximately from just over one month to three to four months.

4.2 Snow reflectance modelling

The RTS kernel was fitted onto the measured snow reflectance data presented in Sect. 2.1. The fitted parameters f_{iso}, f_{vol} and f_{snow} are presented in Fig. 4 for new, hard, and old snow. Coefficient f_{snow} is the most dominant in the SWIR-1 and SWIR-2 wavelengths, while in the NIR band, the isometric coefficient is the most significant. The volumetric coefficient is spectrally close to a constant value for all snow types. It is notable that within the SWIR-2 band, the spectral change in f_{snow} is clearly nonlinear. Example hemispherical plots of the resulting snow BRDF model are presented in Fig. 5 for the three snow types and wavelength bands. For all demonstrations, a systematic enhancement is seen towards more forward-scattering directions as compared to the nadir-view geometry. For all cases, the enhancement is a broad angular feature not limited to the specular

https://doi.org/10.5194/egusphere-2026-2722
Preprint. Discussion started: 21 September 2026

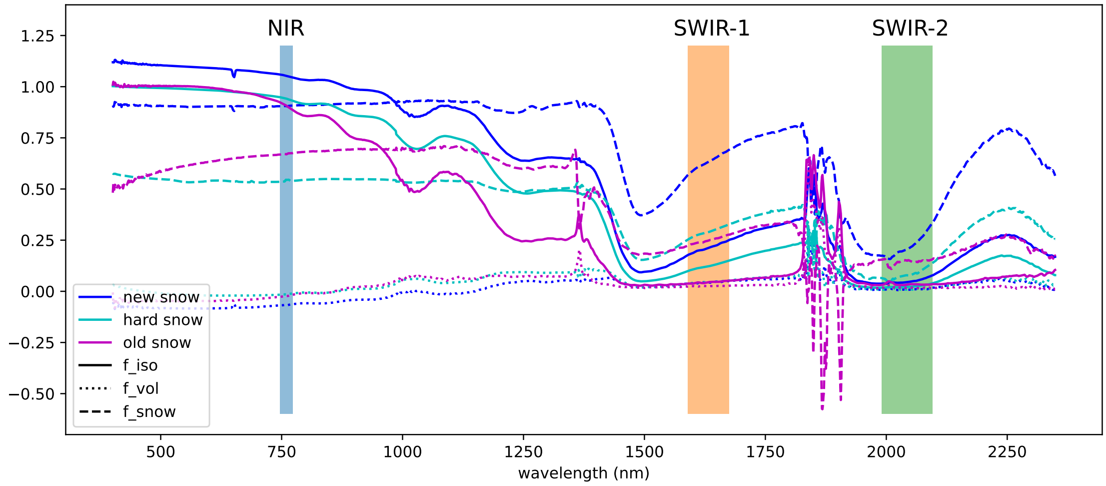

Figure 4. The fitted spectral parameters of the RTS kernel f_{iso}, f_{vol} and f_{snow} are presented for each three snow types. Relevant wavelength bands for the CO_2 retrievals are highlighted.

reflection geometry, contrary to, e.g., glint from water surface. In addition, the enhancement covers a broad azimuthal range, indicating that throughout the CO2M swath width of 250 km, practically no change in the BRDF is expected.

4.3 Simulated top-of-the-atmosphere radiances

We carried out atmospheric RT simulations for the different snow surfaces introduced in Sect. 3.1. The top-of-the-atmosphere (TOA) spectral radiances were simulated in the wavelength bands observed by CO2M. The used RT model input parameters are described in Sect. 3.3.1 The questions of interest driving the needs and the setups for simulations were:

- How variable is the TOA radiance within one full swath in glint mode at the three main bands (NIR, SWIR-1, SWIR-2)?
- How do different snow types affect the spectral radiances in the three bands?
- How does the TOA radiance change with the solar zenith angles and observation modes?
- How does the presence of thin cirrus clouds affect the observed radiance?

The simulation results are presented and analysed in Sects. 4.3.1–4.3.4, following the research questions listed above.

4.3.1 The variability of the TOA radiance from one full swath in glint mode over snow

First, we simulated the top-of-the-atmosphere radiance in all pixels of the full swath over different snow surface types to estimate the variability of the radiance in the swath. The average radiance across the swath and its variability for SZA of

https://doi.org/10.5194/egusphere-2026-2722
Preprint. Discussion started: 21 September 2026

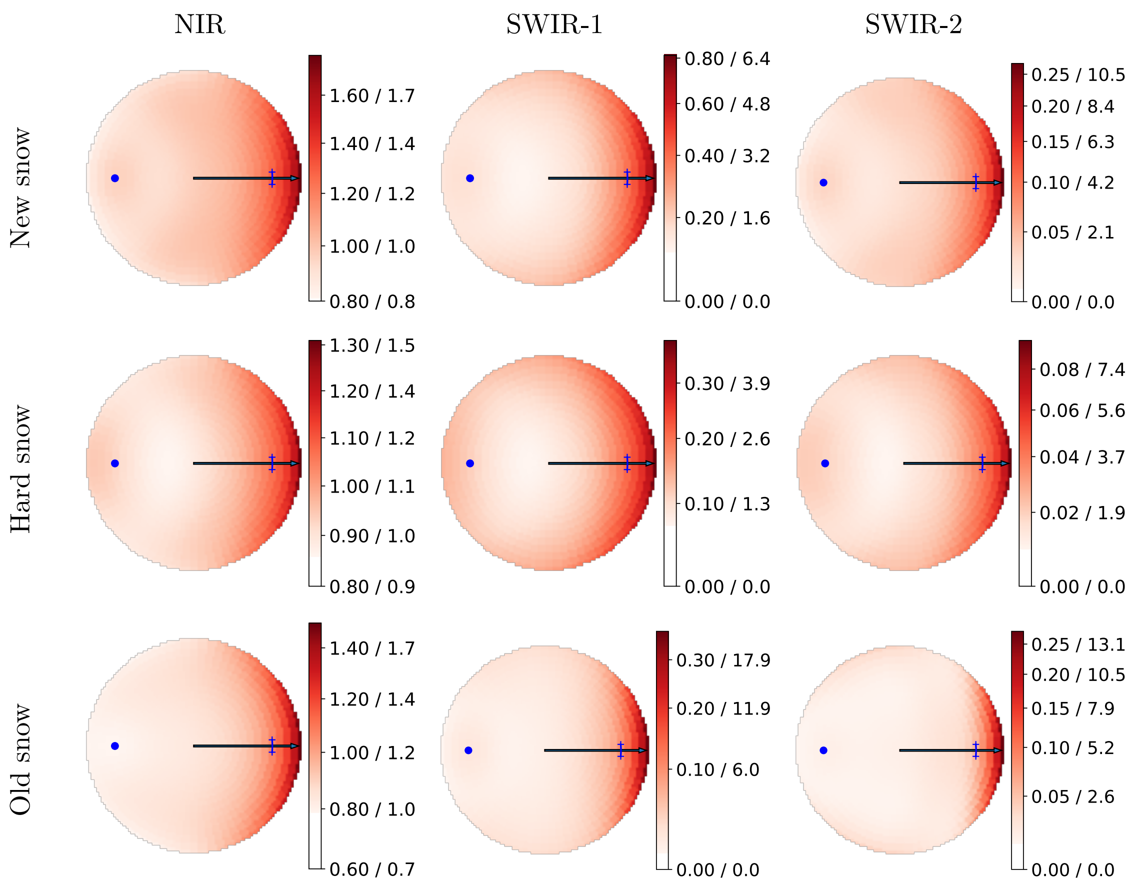

Figure 5. Example hemispherical realisations of the snow surface BRDF models for new snow (top), hard snow (middle) and old snow (bottom) at SZA=58.2°. On the colourbar, the left value is the BRF value and the right value is its ratio to the BRF value at the center of the circle. Note that the color scales differ. The incident radiation is indicated by the blue dot, forward scattering direction is represented with the arrow and the CO2M swath is drawn with a blue line segment at the glint geometry. The zenith angles are limited to 80°.

55 degrees and glint observation geometry are shown in Table 2. The average radiance has been calculated as a mean over all simulated wavelengths within the band. The results show that the NIR band yields the brightest signal as expected based on the snow BRF, and the radiances in the SWIR-1 and SWIR-2 bands are weaker by more than one and two orders of magnitude, respectively. New snow yields the strongest radiances at all three bands while old snow yields systematically the lowest radiances from the three snow types.

The differences in the average radiances across the full swath pixels are very small due to the smooth BRF of snow (see Fig. 5). Based on the minimal variability in the full swath, we conclude that it is sufficient to limit further considerations to selected

https://doi.org/10.5194/egusphere-2026-2722
Preprint. Discussion started: 21 September 2026

Snow type	NIR	SWIR-1	SWIR-2
New snow	212.93 ± 0.25%	13.92 ± 0.48%	0.96 ± 0.61%
Hard snow	182.55 ± 0.16%	7.86 ± 0.31%	0.45 ± 0.50%
Old snow	176.99 ± 0.17%	3.26 ± 1.09%	0.46 ± 1.69%

Table 2. The mean simulated radiance $[\mathrm{mW/m^2/sr/nm}]$ and its variability across the CO2M observation swath in glint geometry over snow at SZA = 55°. The variability is calculated as $(\max(L) - \min(L))/\mathrm{mean}(L) \cdot 100\%$, where L is the swath radiance.

pixels in the swath width. We selected a total of 15 pixels equally distributed across the swath width (including the central pixel and the edge pixels) and refer to this selection as the sub-swath in the following considerations.

4.3.2 The variability of the TOA radiance spectra for different snow types

The spectral radiance of the centre pixel of the swath for different snow surface types and in the different wavelength bands in both nadir ($\theta_v = 0$) and glint ($\theta_v = \theta_s$) observation geometries are shown in Fig. 6. As seen already in Sect. 4.3.1, the radiance levels vary substantially in magnitude in the different bands. In particular, the radiances in the SWIR-1 band are consistently larger than in the SWIR-2 band. The magnitude of the difference depends on the snow type.

Comparing the observed spectral radiances between nadir and glint observation modes, it can be seen that higher radiance levels are consistently observed in the glint geometry. In the NIR band, the effect is not as dramatic as in the SWIR-1 and -2, where the observed TOA radiance is 3–5 times higher in glint mode. This is consistent with the findings by Mikkonen et al. (2024). The spectral radiances are also compared against the (condition-dependent) minimum observable radiance of CO2M, L_{min}, which shows that over snow surfaces, nadir observation mode does not yield almost any signal in SWIR-2 and observability depends on the snow type in SWIR-1, whereas in glint mode the spectra are mostly stronger than the minimum observable radiances in SWIR-2 and stronger for all snow types in SWIR-1.

4.3.3 The dependence of the TOA radiances on the solar zenith angles and observation modes over snow

In addition to the snow type, the observed radiance depends on the geometry of the measurement situation, i.e., the solar zenith and azimuth angles and the viewing zenith and azimuth angles. The solar azimuth angle has been set to a constant value in these simulations as described earlier. Here, we focus on studying the impact of the changing solar zenith angle in the radiance levels in both nadir and glint observation geometries.

The impact of the changing solar zenith angle on the radiances is presented in Fig. 7 for both nadir and glint observations. The simulations were carried out for SZAs of 55, 60, 65, and 70 degrees in both modes. These SZAs represent the extent of encountered solar geometries when CO2M observes the high Northern latitudes during the shoulder seasons. As the atmospheric path length grows with increasing SZA, the nadir radiances decrease due to atmospheric scattering. Conversely, in the SWIR-1 and SWIR-2 bands in the glint mode, the radiances increase with large SZA because of the strong forward-scattering enhancement in the snow BRDF at these wavelengths. This would suggest that in spring, when the SZAs are large and snow

https://doi.org/10.5194/egusphere-2026-2722
Preprint. Discussion started: 21 September 2026

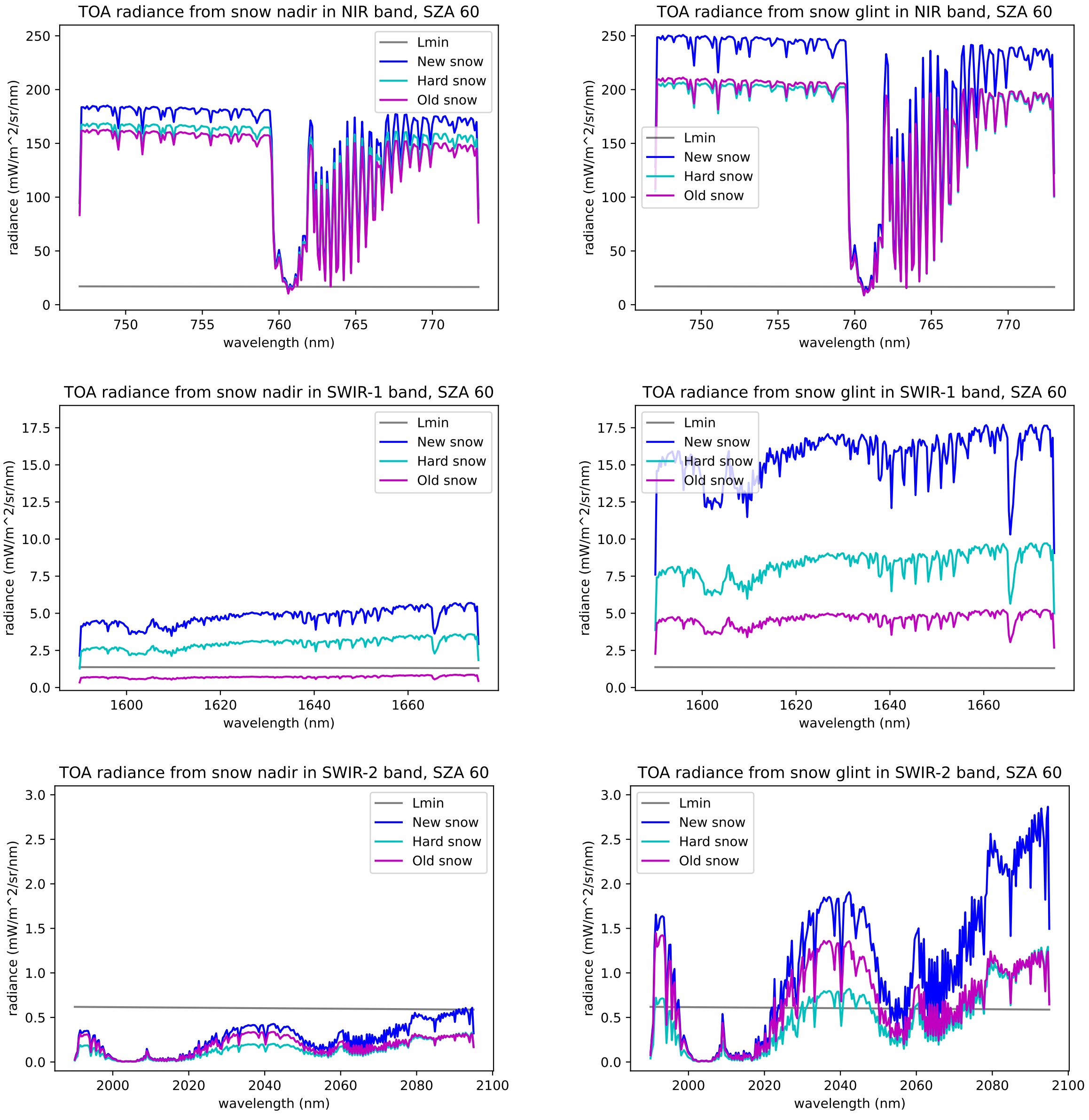

Figure 6. Comparison of the top-of-the-atmosphere radiance simulations for the centre pixel of the CO2M swath at SZA of 60 degrees at nadir observation geometry (left) and glint observation geometry (right) over snow for the NIR band (top), SWIR-1 band (middle), and the SWIR-2 band (bottom). Simulations were carried out for different snow surface types. Lmin indicates the worst case continuum level radiance at 70 degrees SZA as per Table 4.7 in the CO2M MRD (Meijer et al., 2020).

cover still persists at high latitudes, the glint observation geometry would prove to be particularly beneficial for an increased

https://doi.org/10.5194/egusphere-2026-2722
Preprint. Discussion started: 21 September 2026

signal. However, it must be noted that especially for the largest SZAs, multiple scattering in the atmosphere increases, which may complicate the RT modelling as well as the retrieval process.

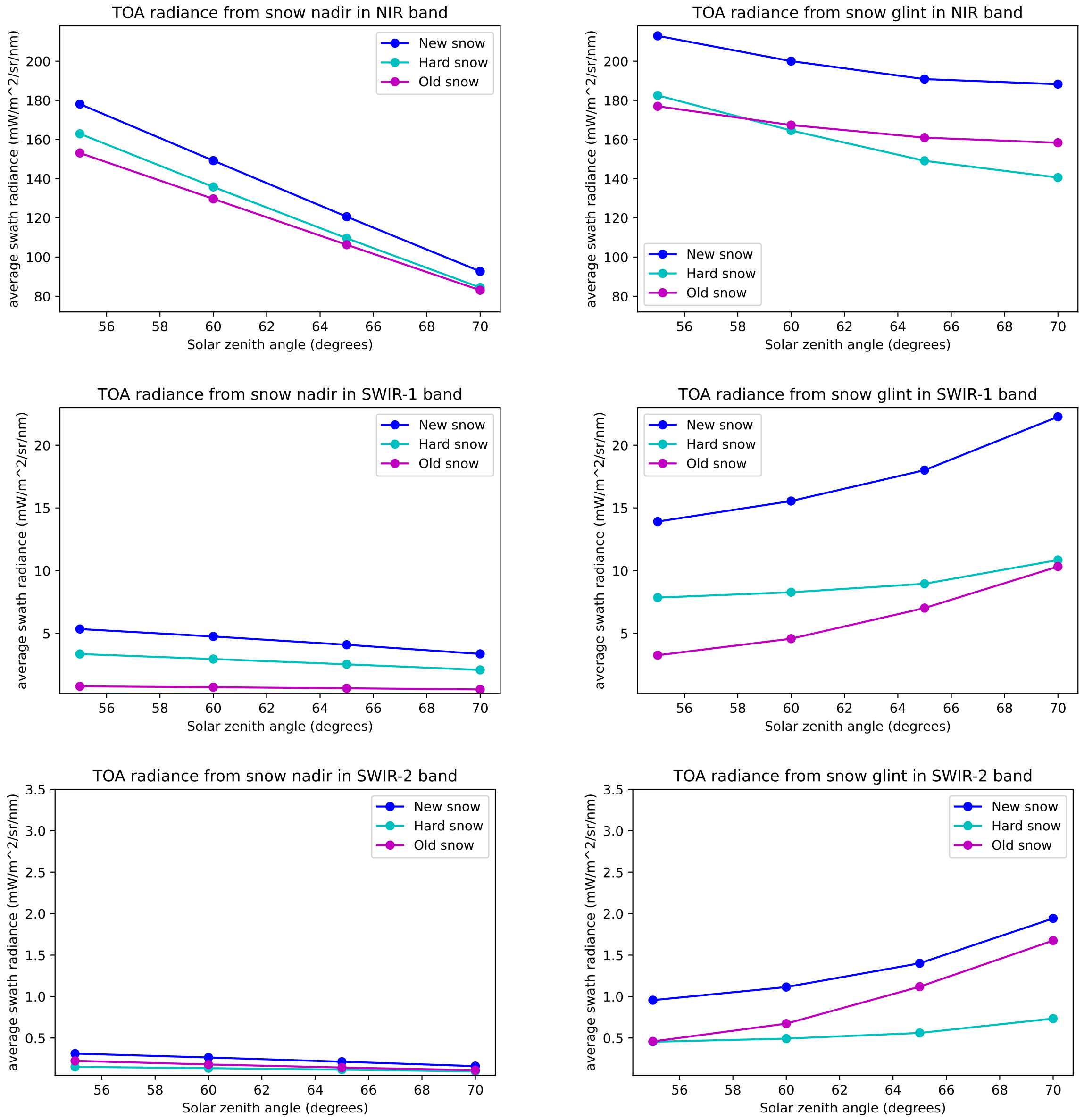

Figure 7. Impact of the solar zenith angle on the top-of-the-atmosphere radiances over snow in nadir (left column) and glint (right column) observation modes.

https://doi.org/10.5194/egusphere-2026-2722
Preprint. Discussion started: 21 September 2026

4.3.4 Effects of ice clouds on the observed radiance

Averaged spectral radiances of swath centre pixels with an optically thin ice crystal cirrus cloud present at 6 km altitude and simulated with Siro is presented in Fig. 8. The clear-sky case as well as the case with a cirrus cloud at 0.75 km altitude are presented in Appendix, Figs. B1 and B2.

We can observe that even thin cirrus clouds cause noticeable multiple scattering in nadir mode and about 3 – 10 times higher contribution of multiple scattering in glint mode across all bands. The contribution of atmospheric scattering increases with the increasing SZA in glint mode, but stays constant in nadir mode. However, the increased glint-mode radiance due to the snow surface reflectance is still visible in the SWIR bands, but it could get masked by the ice clouds. Due to the additional atmospheric scattering with similar spectral characteristics as the snow surface, the presence of the cirrus cloud may obfuscate the observation if it is not taken into account. Cloud of ice crystals also can cause it to be difficult to differentiate surface snow types from each other. This is apparent from the overlapping "blocks" of radiance in Fig. 8. Inferring the correct snow type was found to be of importance for a successful retrieval in Sect. 4.4. These findings indicate that cirrus contamination (i.e., undetected ice clouds) could have significant effects on the optical path of the observation and therefore could result in difficulties, e.g., in the surface pressure retrieval and as such cause large biases in the retrieved XCO_2.

4.4 XCO_2 retrieval tests from simulated data with the UoL-FP framework

Two retrieval experiments described in Sect. 3.4.1 have been carried out to assess performance differences between nadir and glint mode over snow. In the first experiment, we have perturbed the CO_2 a priori profile of the retrieval and we evaluate how well the XCO2 values in the simulations are reproduced over different snow surfaces or nadir and glint observation mode. The difference in XCO_2 between the retrieval and the simulation is given as XCO_2 bias in Fig. 9.

In nadir mode, we find only small XCO_2 biases over new and hard snow with a mean bias of 0.15 ppm or less. The behaviour for old snow is different. For the lower end of SZAs we observe similar values for the mean XCO_2 bias which, however, strongly increases to a negative mean bias of 1.4 ppm for larger SZA. In glint mode and for new and hard snow, we observe very similar results as for nadir mode. For old snow, we find a significant improvement in the retrieval performance. The large mean XCO_2 biases with increasing SZA are not observed in glint mode and all three snow surfaces show similar, small mean XCO_2 biases that vary only little with SZA.

The observed behaviour of XCO_2 biases for nadir and glint retrievals is reflected in the XCO_2 precision given by the a posteriori error (Fig. 10). For nadir mode, we find similar values of the mean XCO_2 precision for new and hard snow with a modest increase with SZA from 0.9 ppm to 1.6 ppm for new snow and 1.0 ppm to 1.9 ppm for hard snow. For old snow, the mean XCO_2 precision is much worse and increases from 1.4 ppm for SZA of 50° to more than 5.5 ppm for SZA of 80°.

Using glint mode leads to a small improvement in XCO_2 precision for low SZA with values of 0.7 ppm and 0.8 ppm for new and hard snow, respectively. The XCO_2 precision further improves with increasing SZA in accordance with the increasing SWIR radiance leading to a clear performance advantage of glint mode in terms of precision for these two snow surfaces. For

https://doi.org/10.5194/egusphere-2026-2722
Preprint. Discussion started: 21 September 2026

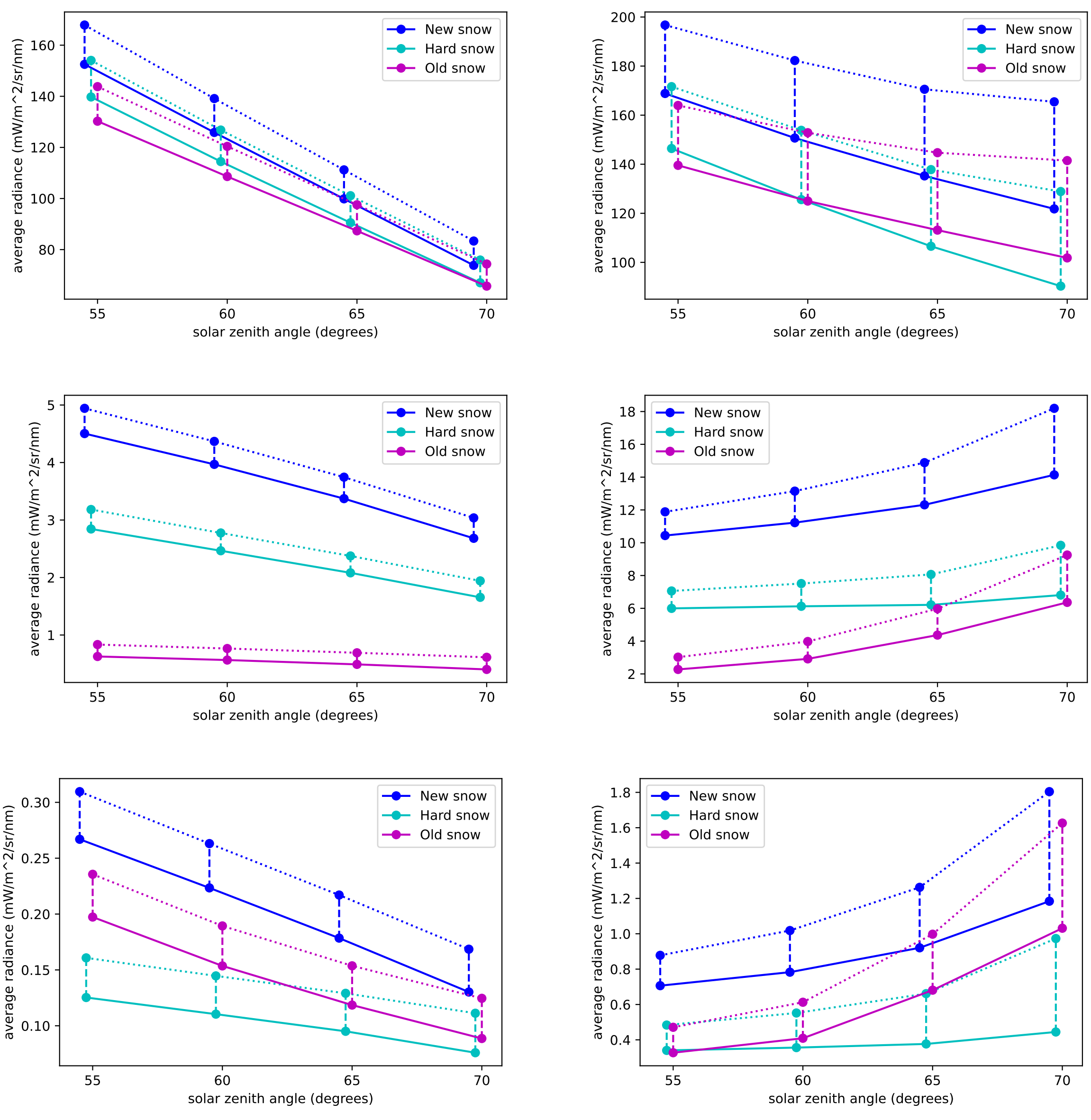

Figure 8. The average spectral radiance over the NIR (top row), SWIR-1 (middle row) and SWIR-2 (bottom row) over different solar zenith angles and snow surfaces in nadir (left column) and glint (right column) observation modes. The ice cloud of 0.05 cloud optical density is at 6 km altitude. The solid line is the contribution of the surface reflectance to the radiance and the dotted line is the total radiance. The dashed line denotes the difference between the two. Different surfaces were simulated using the same solar zenith angles, but they are plotted slightly in different positions due to clarity. Please note the differing y-axes.

https://doi.org/10.5194/egusphere-2026-2722
Preprint. Discussion started: 21 September 2026

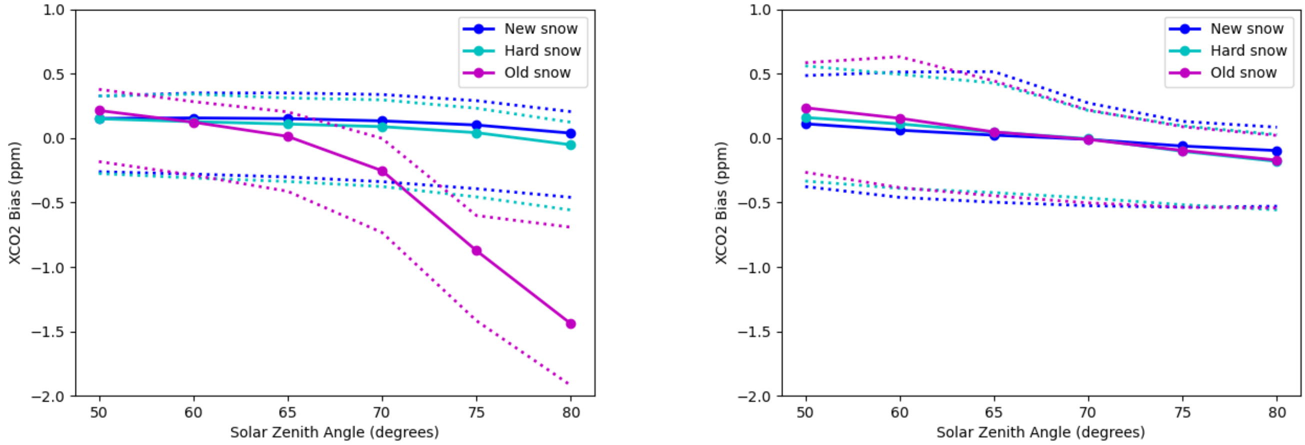

Figure 9. XCO_2 biases for the retrieval over the three different snow surfaces as a function of SZA in nadir (left) and glint (right) mode when perturbing the a priori CO_2 profile of the retrieval. The thick solid lines give the mean and the dotted lines the upper and lower limit.

the case of old snow, improvement of the XCO_2 precision in glint mode are dramatic and the XCO_2 precision now ranges from 0.9 ppm for 50° to 0.6 ppm for 80°.

We also investigated the impact of surface BRDF assumption for the retrievals over snow surfaces in nadir and glint mode (Fig. 11). To do so, we retrieved XCO_2 from spectra simulated for old snow using hard and new snow assumptions. For nadir mode, we find that the mean XCO_2 biases are small for low SZA and increase with SZA to 0.5 and 0.9 ppm. The range of biases increases substantially with SZA and the upper and lower limit of the XCO_2 biases have an absolute value as large as 3 ppm at large SZA. In glint mode, the mean XCO_2 bias is slightly smaller than in nadir mode and are less than 0.2 ppm for hard snow and less than 0.6 ppm for new snow. Also in glint mode, we find a large range of XCO_2 biases which is much lower for hard snow and the SZA dependence is less pronounced.

5 Discussion

To evaluate the relevance of snow surfaces for the CO2M mission, statistical and geographical analysis of snow extent was carried out at Northern high latitudes. Figure 1 demonstrates that snow surfaces are widely present over high latitudes through the spring months from March to May. Considering the CO2M mission requirements for making retrievals of XCO_2 at SZA < 70°, we can conclude based on Fig. 3 that while the SZA can be a limiting factor for retrievals in the winter months, this is no longer the case after February for the highest latitudes considered here (68°N), and earlier at lower latitudes. Snow, on the other hand, can persist at high latitudes until late May. This means that snow cover and the start of the photosynthesis in boreal forests occur simultaneously, which highlights the importance of successful XCO_2 satellite observations to correctly

https://doi.org/10.5194/egusphere-2026-2722
Preprint. Discussion started: 21 September 2026

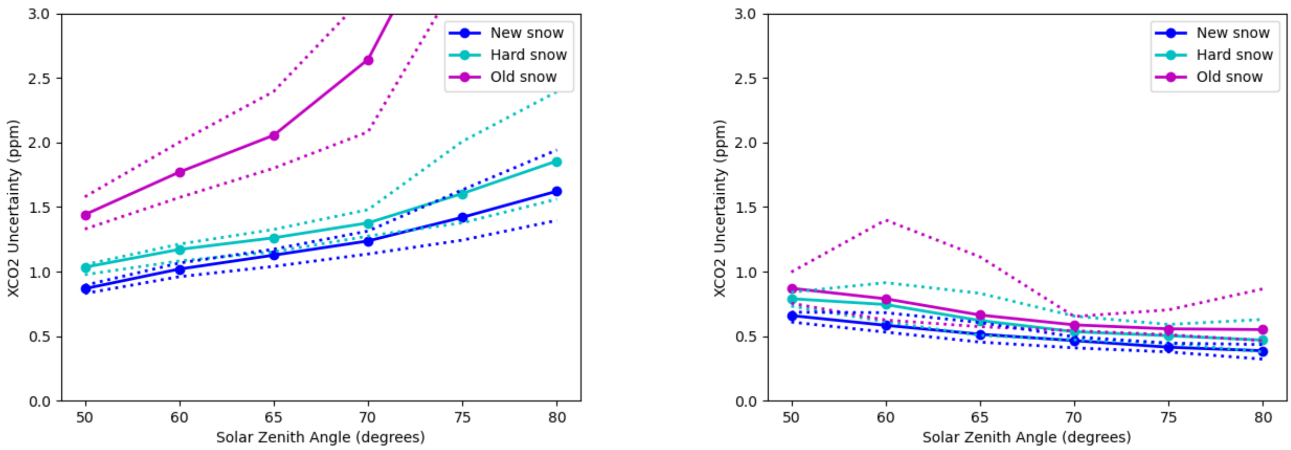

Figure 10. XCO_2 uncertainty (a posteriori error) for the retrieval over the three different snow surfaces as a function of SZA in nadir (left) and glint (right) mode. The thick solid lines give the mean and the dotted lines the upper and lower limit.

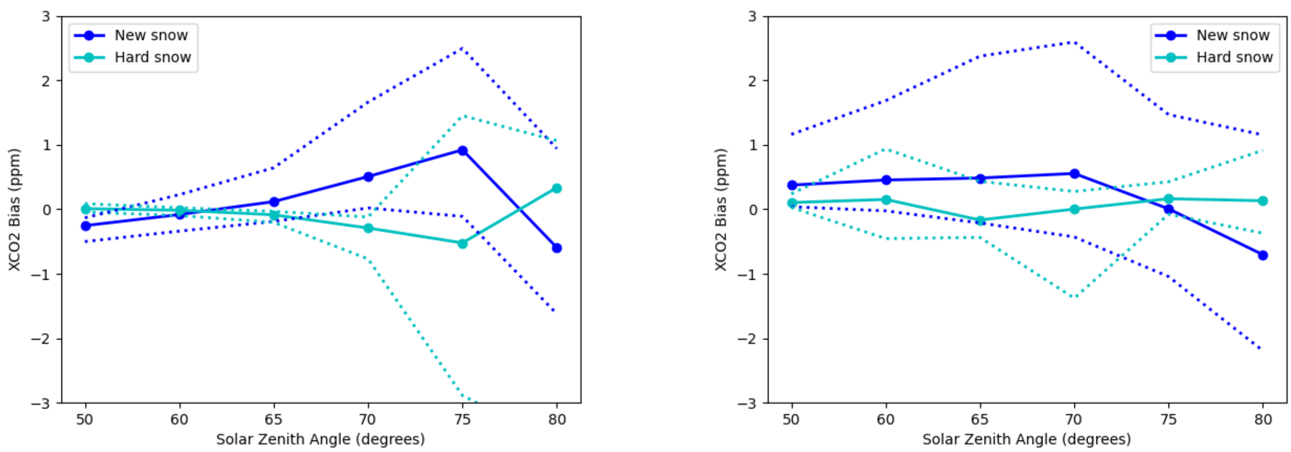

Figure 11. XCO_2 biases for the simulations for old snow but retrieved with new snow or hard snow BRDF in nadir (left) and glint (right) mode.

https://doi.org/10.5194/egusphere-2026-2722
Preprint. Discussion started: 21 September 2026

track the seasonal cycle of XCO_2 and thereby carbon uptake. This would enable and support the CO2M mission to achieve its mission objectives for tracking anthropogenic emissions also at high latitudes, and improve tracking of emissions and removals from the land use, land use change, and forestry (LULUCF) sector, which contains large uncertainties for example in Nordic countries (e.g., Isomäki et al., 2024).

For the RT model simulations and retrieval tests, a model for the snow surface reflectance at the NIR, SWIR-1, and SWIR-2 wavelength bands was necessary. The goniometer measurement database covered these bands but some gaps remained in the angular range of the measured data. After experimenting with Legendre polynomial modelling techniques utilized by Mikkonen et al. (2024) and testing with kernel models, it turned out that the RTS kernel model performed most reliably for the extrapolation over the angular range of the hemisphere. The isotropic and snow kernels showed large spectral variability, while the volumetric kernel shows small values throughout the NIR-SWIR bands. The spectral dependence of the kernels was found to be similar for new snow, hard snow, and old snow, but a systematic difference was found in the kernel values of the three snow types. While real snow surface types are not limited to three, these types can be considered as a representative collection of the snow types that are common especially in the spring months, which were found to yield the highest potential for improved CO2M observations over snow.

The radiative transfer simulations over snow were carried out in order to simulate the observable top-of-the-atmosphere radiance levels of the CO2M mission and to inform mission operations planning on the differences between the nadir and glint observing geometries in terms of simulated radiances and, furthermore, testing the retrievals of XCO_2 over snow. Based on the RT simulations, the glint observation geometry yielded higher radiances than the nadir geometry for all snow surface types tested, and at all three bands. This suggests that conducting satellite observations of these three spectral bands over snow surfaces would be preferable in glint mode rather than in nadir mode.

Using retrieval experiments with the UoL-FP retrieval algorithm of simulated CO2M-like spectra over snow, we showed that there is a clear performance gain in the XCO_2 retrieval in glint mode over nadir mode over snow surfaces. This was most pronounced for old snow where TOA radiances are very low in the SWIR bands in nadir mode resulting in high retrieval uncertainties and low information content. However, assumptions on snow type matter and a wrong snow BRDF can result in XCO_2 biases of up to 2–3 ppm in both nadir and glint mode.

The results of our study are specific to XCO_2 but can also point to few remarks about satellite-based total column methane (XCH_4) retrievals over snow. Based on the BRDF measurements, snow surface reflectance is lower for the CO_2 absorption bands than for CH_4 absorption bands which highlights the challenges for the CO_2 retrieval over snow. A forward enhancement in reflectance is also present in the CH_4 bands and thus the improvements found for CO_2 suggest also an improvement for CH_4 retrievals. A recent evaluation of Sentinel-5P TROPOMI XCH_4 retrievals over Northern high latitudes by Lindqvist et al. (2024) indicates that the retrievals have good coverage also over snow-covered time, and that the accuracy and precision against ground-based references do not indicate an obvious snow-related bias for XCH_4 retrievals. Still, the improvements found in our work for XCO_2 retrievals (regarding, e.g., the inclusion of a BRDF model) are also applicable to XCH_4 while they may not be as necessary.

https://doi.org/10.5194/egusphere-2026-2722
Preprint. Discussion started: 21 September 2026

6 Conclusions

Snow coverage is one of several challenges in making reliable space-based observations of total column carbon dioxide (XCO_2) in the shortwave-infrared wavelengths over Northern high latitudes. In this research, we modelled the reflectance of solar radiation over snow in the NIR-SWIR wavelength bands in order to simulate more realistically the top-of-the-atmosphere radiances at these wavelengths and further test the feasibility of XCO_2 satellite retrievals over snow. Our tests were carried out for the Copernicus Anthropogenic CO_2 Monitoring (CO2M) mission, with the aim of providing guidance to the design of the mission operations concept on an optimal operation mode for snow-covered regions.

The key result of our study is that glint-mode observations were shown to lead to higher signal-to-noise ratios and improved retrievals in terms of reduced errors compared to the nadir geometry in the Northern high latitudes (i.e. large solar zenith angles) over snow. Based on Mikkonen et al. (2024), the signal-to-noise ratio increases towards forward-scattering direction until large air masses counteract the benefit of increased reflectance, which indicates that the exact specular reflection (glint) geometry is not required but forward scattering directions in general have advantages at large solar zenith angles. Our results do not point to any single SZA limit to when the glint-viewing direction would be preferable to nadir viewing, but it seems that at SZA$>60°$the benefits are the most obvious.

We found that the improvements attained are conditional to a well-constrained snow BRDF. Therefore, a good knowledge of the snow reflectance and its angular dependence is essential. While the snow BRDF model in this work is based on long-term snow measurements with a field goniospectrometer, upscaling the observed 10×10 cm^2 ground pixel to the satellite's 2×2 km^2 spatial sample as well as considering the effects of vegetation and surface topography induce uncertainties. Spectral validation of the snow BRDF model in larger scale for example by using drone-borne or tower-based spectrometer observations in these wavelengths is important prior to a wider application of the snow BRDF model. It should be emphasized that the wavelength bands in the NIR-SWIR spectral region investigated in this work have been little covered in snow-related research due to their low information content regarding snow properties, and therefore additional field research can help test and validate the model. Furthermore, CO2M will be equipped with a multi-angle polarimeter instrument and a cloud imager instrument which could be used for additional constraining of the surface BRDF, or the detection of optically thin cirrus clouds.

Although this research suggests that XCO_2 satellite retrievals over snow can be improved by considering a snow BRDF model and forward-scattered radiation instead of nadir geometry, the resulting improvements are limited to cloud-free situations with sufficient solar elevation. To fully cover the observational winter gap due to insufficient solar radiation in Northern high latitudes, active space-based measurements or observations in the thermal infrared wavelengths are necessary. On the other hand, the potential 1-3 months' extension of the spring observational coverage to consider snow surfaces as pointed out by our study could be crucial in better constraining the maximum of the XCO_2 seasonal cycle and thereby the seasonal cycle amplitude that is strongly linked to the biospheric CO_2 fluxes. The impact of the extended temporal coverage and enhanced seasonal cycle amplitude constraints are beyond the scope of this study but could be investigated for example through an Observing System Simulation Experiment (OSSE) or with existing OCO-2 satellite observations.

https://doi.org/10.5194/egusphere-2026-2722
Preprint. Discussion started: 21 September 2026

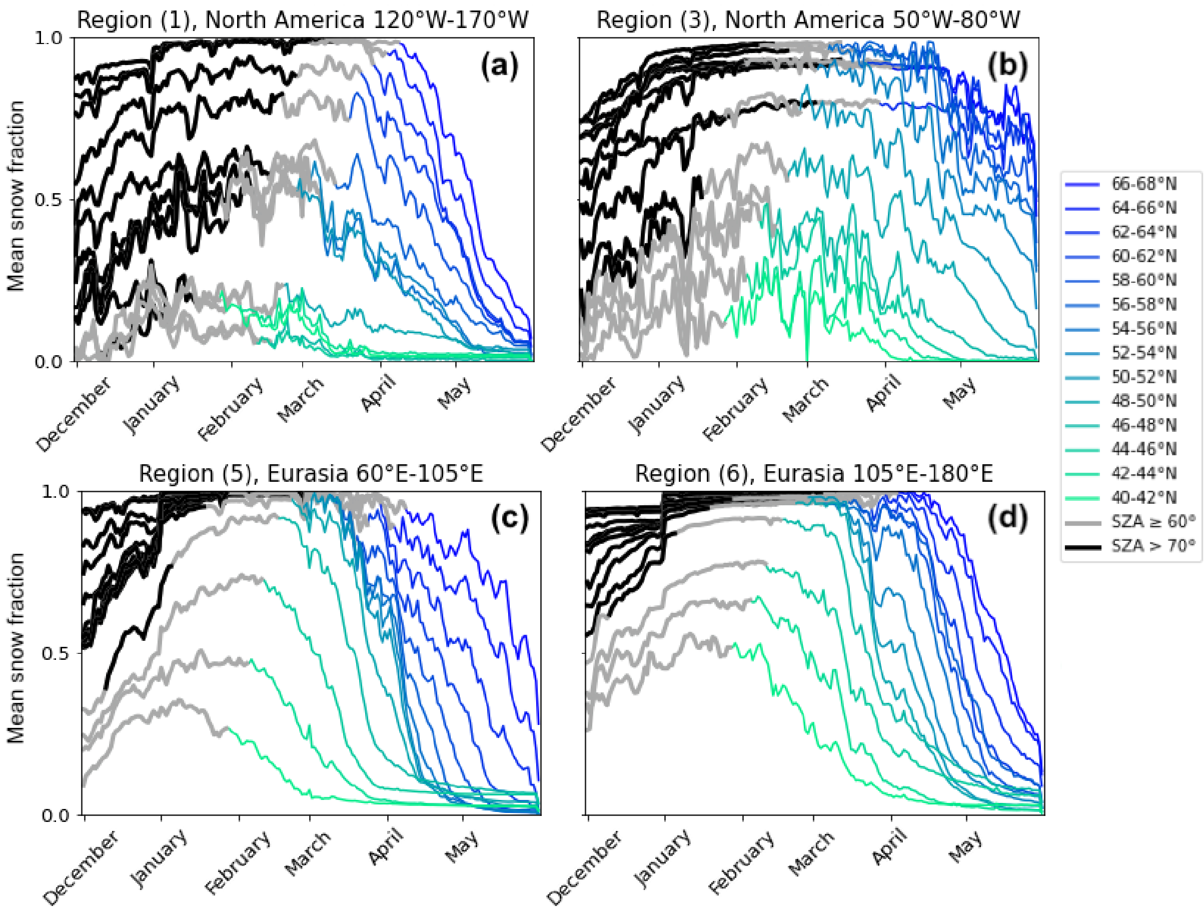

Figure A1. Mean snow fraction for (a) the westernmost North American study area (Area 1 in Fig. 1), (b) the easternmost North American study area (Area 3), (c) the central Eurasian study area (Area 5), and (d) the easternmost Eurasian study area (Area 6), averaged over the years 2012–2018. Each line represents one latitude zone, and the lines are coloured according to the latitude zones. Gray and black lines in the latitude zones denote periods when SZA exceeds 60° and 70° at 11:30 local time.

Code and data availability. The GlobSnow v3.0 Snow Water Equivalent data product is available at https://www.globsnow.info/swe/archive_v3.0/. The radiative transfer models Raysca and Siro are available at https://github.com/amikko/arsca. Any other data, models or codes are available upon request.

Appendix A: Snow coverage figures

The snow fraction for each latitude band as a function of time for regions 1, 3, 5 and 6 of Fig. 1 is presented in Fig. A1.

https://doi.org/10.5194/egusphere-2026-2722
Preprint. Discussion started: 21 September 2026

Appendix B: Simulated radiances over snow with atmospheric ice crystals

The simulated single- and multiple scattering radiances as a function of the solar zenith angle in are presented in Fig. B1, with no ice cloud present, and B2, with an ice cloud at 0.75 km altitude.

Author contributions. HL and YM planned the study. JP and MG provided the snow reflectance measurement data, and JP and AM created the snow BRDF models based on them. EK and MS curated and analyzed the snow coverage data. AM carried out the radiative transfer simulation experiments, for which HL provided the ice crystal scattering data. HB, LV and AdN carried out the retrieval experiments. HL was responsible of funding acquisition and project management. HL supervised AM and EK. AM, HL, HB, JP, EK, MS, AdN, and YM prepared the original manuscript draft. All authors provided comments on the manuscript.

Competing interests. The authors declare no competing interests.

Acknowledgements. We acknowledge Dr. Janne Hakkarainen, Dr. Tomi Karppinen, and Dr. Rigel Kivi for their contributions to the SNOWITE project. The OCO-2 Northern High Latitudes project team, led by Dr. Abhishek Chatterjee, is acknowledged for fruitful collaboration. The research was funded by the European Space Agency's project "Study on improved glint retrieval for the CO2M" (Contract 4000133991/21/NL/FF/ab; FMI-SNOWITE) and Research Council of Finland (grant agreements 336798, 337552, 331829, 350184, 353082, 364975, and 359196).

https://doi.org/10.5194/egusphere-2026-2722
Preprint. Discussion started: 21 September 2026

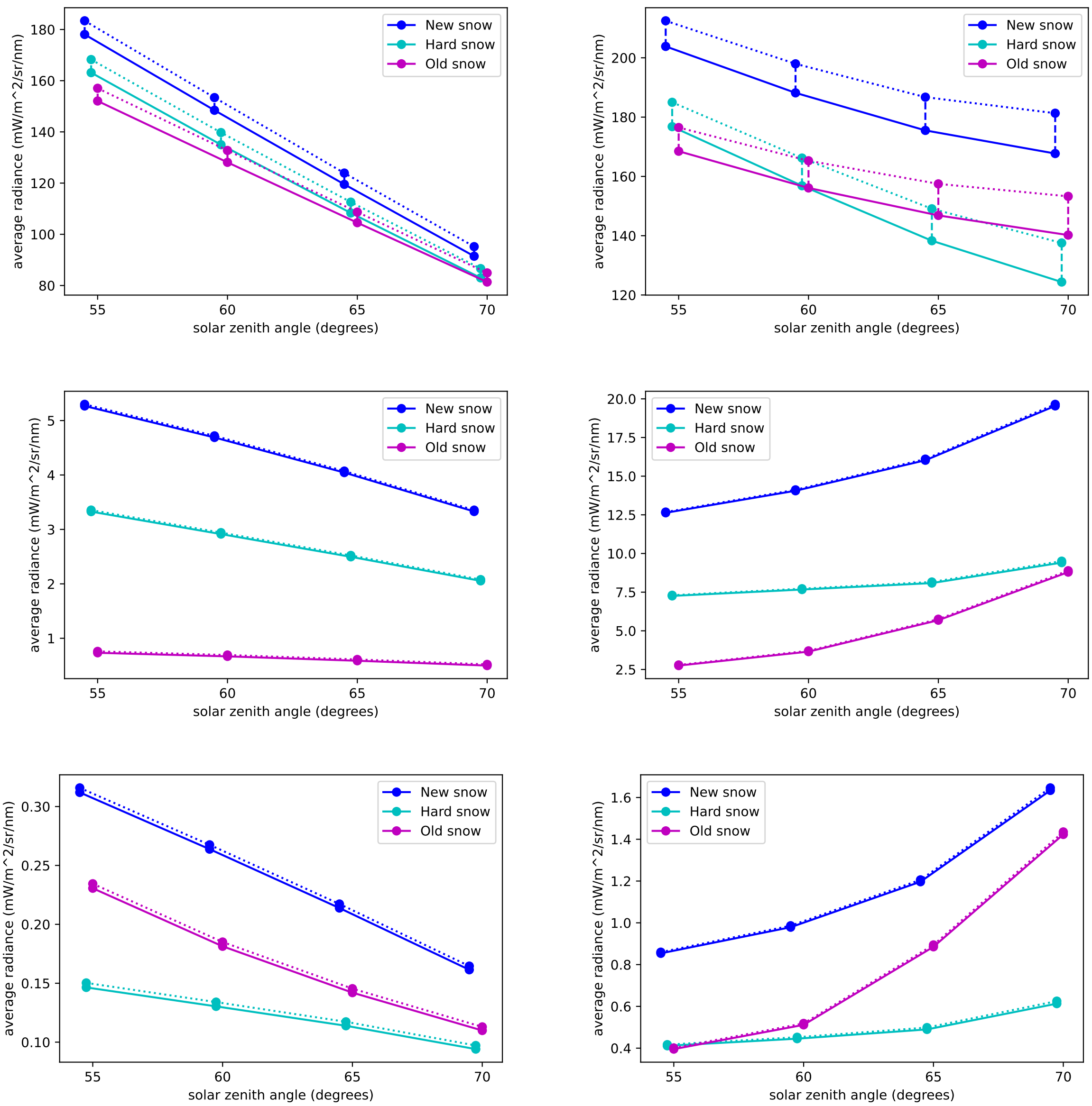

Figure B1. The average spectral radiance over the NIR (top row), SWIR-1 (middle row) and SWIR-2 (bottom row) over different solar zenith angles and snow surfaces in nadir (left column) and glint (right column) observation modes. No ice cloud is present. The solid line is the contribution of the surface reflectance to the radiance and the dotted line is the total radiance. The dashed line denotes the difference between the two. Different surfaces were simulated using the same solar zenith angles, but they are plotted slightly in different positions due to clarity.

https://doi.org/10.5194/egusphere-2026-2722
Preprint. Discussion started: 21 September 2026

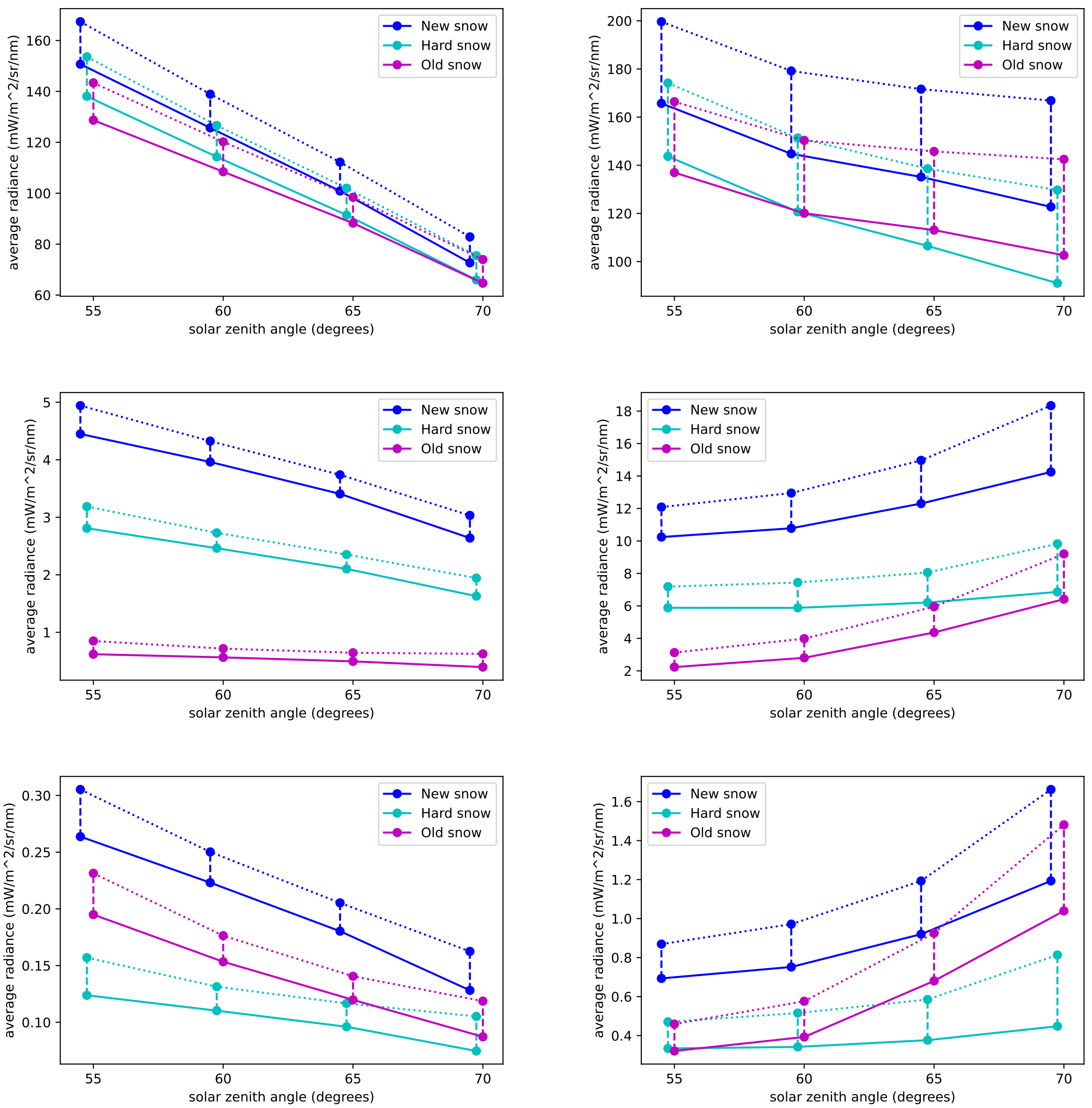

Figure B2. The average spectral radiance over the NIR (top row), SWIR-1 (middle row) and SWIR-2 (bottom row) over different solar zenith angles and snow surfaces in nadir (left column) and glint (right column) observation modes. The ice cloud of 0.05 cloud optical density is at 0.75 km altitude. The solid line is the contribution of the surface reflectance to the radiance and the dotted line is the total radiance. The dashed line denotes the difference between the two. Different surfaces were simulated using the same solar zenith angles, but they are plotted slightly in different positions due to clarity.

https://doi.org/10.5194/egusphere-2026-2722
Preprint. Discussion started: 21 September 2026

References

Baum, B. A., Yang, P., Heymsfield, A. J., Bansemer, A., Cole, B. H., Merrelli, A., Schmitt, C., and Wang, C.: Ice cloud single-scattering property models with the full phase matrix at wavelengths from 0.2 to 100 μm, Journal of Quantitative Spectroscopy and Radiative Transfer, 146, 123–139, 2014.

Boesch, H., Baker, D.and Connor, B., Crisp, D., and Miller, C.: Global Characterization of CO2 Column Retrievals from Shortwave-Infrared Satellite Observations of the Orbiting Carbon Observatory-2 Mission, Remote Sensing, 3, 270–304, https://doi.org/10.3390/rs3020270, 2011.

Byrne, B., Liu, J., Yi, Y., Chatterjee, A., Basu, S., Cheng, R., Doughty, R., Chevallier, F., Bowman, K. W., Parazoo, N. C., Crisp, D., Li, X., Xiao, J., Sitch, S., Guenet, B., Deng, F., Johnson, M. S., Philip, S., McGuire, P. C., and Miller, C. E.: Multi-year observations reveal a larger than expected autumn respiration signal across northeast Eurasia, Biogeosciences, 19, 4779–4799, https://doi.org/10.5194/bg-19-4779-2022, 2022.

Byrne, B., Baker, D. F., Basu, S., Bertolacci, M., Bowman, K. W., Carroll, D., Chatterjee, A., Chevallier, F., Ciais, P., Cressie, N., Crisp, D., Crowell, S., Deng, F., Deng, Z., Deutscher, N. M., Dubey, M. K., Feng, S., García, O. E., Griffith, D. W. T., Herkommer, B., Hu, L., Jacobson, A. R., Janardanan, R., Jeong, S., Johnson, M. S., Jones, D. B. A., Kivi, R., Liu, J., Liu, Z., Maksyutov, S., Miller, J. B., Miller, S. M., Morino, I., Notholt, J., Oda, T., O'Dell, C. W., Oh, Y.-S., Ohyama, H., Patra, P. K., Peiro, H., Petri, C., Philip, S., Pollard, D. F., Poulter, B., Remaud, M., Schuh, A., Sha, M. K., Shiomi, K., Strong, K., Sweeney, C., Té, Y., Tian, H., Velazco, V. A., Vrekoussis, M., Warneke, T., Worden, J. R., Wunch, D., Yao, Y., Yun, J., Zammit-Mangion, A., and Zeng, N.: National CO_2 budgets (2015–2020) inferred from atmospheric CO_2 observations in support of the global stocktake, Earth System Science Data, 15, 963–1004, https://doi.org/10.5194/essd-15-963-2023, 2023.

Chatterjee, A., Gierach, M., Sutton, A., Feely, R., Crisp, D., Eldering, A., Gunson, M., O'Dell, C., Stephens, B., and Schimel, D.: Influence of El Niño on atmospheric CO_2 over the tropical Pacific Ocean: Findings from NASA's OCO-2 mission, Science, 358, eaam5776, 2017.

Cogan, A. J., Boesch, H., Parker, R. J., Feng, L., Palmer, P. I., Blavier, J.-F. L., Deutscher, N. M., Macatangay, R., Notholt, J., Roehl, C., Warneke, T., and Wunch, D.: Atmospheric carbon dioxide retrieved from the Greenhouse gases Observing SATellite (GOSAT): Comparison with ground-based TCCON observations and GEOS-Chem model calculations, Journal of Geophysical Research: Atmospheres, 117, https://doi.org/https://doi.org/10.1029/2012JD018087, 2012.

Crisp, D., Atlas, R. M., Breon, F.-M., Brown, L., Burrows, J., Ciais, P., Connor, B., Doney, S., Fung, I., Jacob, D., et al.: The Orbiting Carbon Observatory (OCO) mission, Advances in Space Research, 34, 700–709, 2004.

Ding, A., Jiao, Z., Dong, Y., Zhang, X., Peltoniemi, J. I., Mei, L., Guo, J., Yin, S., Cui, L., Chang, Y., and Xie, R.: Evaluation of the Snow Albedo Retrieved from the Snow Kernel Improved the Ross-Roujean BRDF Model, Remote Sensing, 11, https://doi.org/10.3390/rs11131611, 2019.

Hannula, H.-R., Heinilä, K., Böttcher, K., Mattila, O.-P., Salminen, M., and Pulliainen, J.: Laboratory, field, mast-borne and airborne spectral reflectance measurements of boreal landscape during spring, Earth System Science Data, 12, 719–740, 2020.

Isomäki, K., McGrath, M. J., Backman, L., Leskinen, J., Berchet, A., Broquet, G., Fortems-Cheiney, A., Junttila, V., Leppänen, A., Lindqvist, H., et al.: Assessing the role of terrestrial ecosystems in Finland's total CO_2 balance through a comparison of top-down and bottom-up estimates, Boreal Environment Research, 29, 77–102, 2024.

Jacobs, N., Simpson, W. R., Wunch, D., O'Dell, C. W., Osterman, G. B., Hase, F., Blumenstock, T., Tu, Q., Frey, M., Dubey, M. K., Parker, H. A., Kivi, R., and Heikkinen, P.: Quality controls, bias, and seasonality of CO_2 columns in the boreal forest with Orbiting Carbon

Observatory-2, Total Carbon Column Observing Network, and EM27/SUN measurements, Atmospheric Measurement Techniques, 13, 5033–5063, https://doi.org/10.5194/amt-13-5033-2020, 2020.

Jacobs, N., O'Dell, C. W., Taylor, T. E., Logan, T. L., Byrne, B. K., Kiel, M., Kivi, R., Heikkinen, P., Merrelli, A., Payne, V. H., et al.: The importance of digital elevation model accuracy in XCO_2 retrievals: improving the OCO-2 ACOS v11 product, Atmospheric Measurement Techniques Discussions, 2023, 1–41, 2023.

Janssens-Maenhout, G., Pinty, B., Dowell, M., Zunker, H., Andersson, E., Balsamo, G., Bézy, J.-L., Brunhes, T., Bösch, H., Bojkov, B., et al.: Toward an operational anthropogenic CO_2 emissions monitoring and verification support capacity, Bulletin of the American Meteorological Society, 101, E1439–E1451, 2020.

Jeong, S.-J., Bloom, A. A., Schimel, D., Sweeney, C., Parazoo, N. C., Medvigy, D., Schaepman-Strub, G., Zheng, C., Schwalm, C. R., Huntzinger, D. N., et al.: Accelerating rates of Arctic carbon cycling revealed by long-term atmospheric CO_2 measurements, Science Advances, 4, eaao1167, 2018.

Kivi, R., Heikkinen, P., and Kyrö, E.: TCCON data from Sodankylä (FI), Release GGG2020.R0, https://doi.org/10.14291/tccon.ggg2020.sodankyla01.R0, 2022.

Kochanov, R. V., Gordon, I., Rothman, L., Wcisło, P., Hill, C., and Wilzewski, J.: HITRAN Application Programming Interface (HAPI): A comprehensive approach to working with spectroscopic data, Journal of Quantitative Spectroscopy and Radiative Transfer, 177, 15–30, 2016.

Lindqvist, H., O'Dell, C. W., Basu, S., Boesch, H., Chevallier, F., Deutscher, N., Feng, L., Fisher, B., Hase, F., Inoue, M., et al.: Does GOSAT capture the true seasonal cycle of carbon dioxide?, Atmospheric Chemistry and Physics, 15, 13 023–13 040, 2015.

Lindqvist, H., Martikainen, J., Räbinä, J., Penttilä, A., and Muinonen, K.: Ray optics for absorbing particles with application to ice crystals at near-infrared wavelengths, Journal of Quantitative Spectroscopy and Radiative Transfer, 217, 329–337, 2018.

Lindqvist, H., Kivimäki, E., Häkkilä, T., Tsuruta, A., Schneising, O., Buchwitz, M., Lorente, A., Martinez Velarte, M., Borsdorff, T., Alberti, C., Backman, L., Buschmann, M., Chen, H., Dubravica, D., Hase, F., Heikkinen, P., Karppinen, T., Kivi, R., McGee, E., Notholt, J., Rautiainen, K., Roche, S., Simpson, W., Strong, K., Tu, Q., Wunch, D., Aalto, T., and Tamminen, J.: Evaluation of Sentinel-5P TROPOMI Methane Observations at Northern High Latitudes, Remote Sensing, 16, https://doi.org/10.3390/rs16162979, 2024.

Luojus, K., Pulliainen, J., Takala, M., Lemmetyinen, J., Mortimer, C., Derksen, C., Mudryk, L., Moisander, M., Hiltunen, M., Smolander, T., Ikonen, J., Cohen, J., Salminen, M., Norberg, J., Veijola, K., and Venäläinen, P.: GlobSnow v3.0 Northern Hemisphere snow water equivalent dataset, Scientific Data, 8, https://doi.org/10.1038/s41597-021-00939-2, 2021.

Meier, W. N., Hovelsrud, G. K., Van Oort, B. E., Key, J. R., Kovacs, K. M., Michel, C., Haas, C., Granskog, M. A., Gerland, S., Perovich, D. K., et al.: Arctic sea ice in transformation: A review of recent observed changes and impacts on biology and human activity, Reviews of Geophysics, 52, 185–217, 2014.

Meijer, Y., Bösch, H., Bombelli, A., Brunner, D., Buchwitz, M., Ciais, P., Crisp, D., Engelen, R., Holmund, K., Houweling, S., Janssen-Maenhout, G., Marshall, J., Nakajima, M., Pinty, B., Scholze, M., Bezy, J., Drinkwater, M., Fehr, T., Fernandez, V., Löscher, A., Nett, H., Sierk, B., Dubovik, O., Landgraf, J., Lang, R., Lindqvist, H., Tamminen, J., and Veefkind, P.: Copernicus CO_2 Monitoring Mission Requirements Document, https://esamultimedia.esa.int/docs/EarthObservation/CO2M_MRD_v3.0_20201001_Issued.pdf, 2020.

Meijer, Y., Andersson, E., Boesch, H., Dubovik, O., Houweling, S., Landgraf, J., Lang, R., and Lindqvist, H.: Editorial: Anthropogenic emission monitoring with the Copernicus CO2 monitoring mission, Frontiers in Remote Sensing, 4, https://doi.org/10.3389/frsen.2023.1217568, 2023.

https://doi.org/10.5194/egusphere-2026-2722
Preprint. Discussion started: 21 September 2026

Mikkonen, A., Lindqvist, H., Peltoniemi, J., and Tamminen, J.: Non-Lambertian snow surface reflection models for simulated top-of-the-atmosphere radiances in the NIR and SWIR wavelengths, Journal of Quantitative Spectroscopy and Radiative Transfer, 315, 108 892, 2024.

Mikkonen, A., Koskinen, A., Tamminen, J., and Lindqvist, H.: Scattering graph method for 3D radiative transfer, Opt. Express, 33, 35 489–35 509, https://doi.org/10.1364/OE.562216, 2025.

Natraj, V., Boesch, H., Spurr, R. J. D., and Yung, Y. L.: Retrieval of from simulated Orbiting Carbon Observatory measurements using the fast linearized R-2OS radiative transfer model, Journal of Geophysical Research: Atmospheres, 113, https://doi.org/https://doi.org/10.1029/2007JD009017, 2008.

O'Dell, C. W.: Acceleration of multiple-scattering, hyperspectral radiative transfer calculations via low-streams interpolation, Journal of Geophysical Research: Atmospheres, 115, https://doi.org/https://doi.org/10.1029/2009JD012803, 2010.

O'Dell, C. W., Eldering, A., Wennberg, P. O., Crisp, D., Gunson, M. R., Fisher, B., Frankenberg, C., Kiel, M., Lindqvist, H., Mandrake, L., et al.: Improved retrievals of carbon dioxide from Orbiting Carbon Observatory-2 with the version 8 ACOS algorithm, Atmospheric Measurement Techniques, 11, 6539–6576, 2018.

Oikarinen, L.: Polarization of light in UV-visible limb radiance measurements, Journal of Geophysical Research: Atmospheres, 106, 1533–1544, 2001.

Oikarinen, L.: Effect of surface albedo variations on UV-visible limb scattering measurements of the atmosphere, Journal of Geophysical Research: Atmospheres, 107, https://doi.org/10.1029/2001JD001492, 2002.

Oikarinen, L., Sihvola, E., and Kyrölä, E.: Multiple scattering radiance in limb-viewing geometry, Journal of Geophysical Research: Atmospheres, 104, 31 261–31 274, https://doi.org/10.1029/1999JD900969, 1999.

Palmer, P. I., Feng, L., Baker, D., Chevallier, F., Bösch, H., and Somkuti, P.: Net carbon emissions from African biosphere dominate pan-tropical atmospheric CO2 signal, Nature Communications, 10, 3344, 2019.

Peltoniemi, J., Hakala, T., Suomalainen, J., and Puttonen, E.: Polarised bidirectional reflectance factor measurements from soil, stones, and snow, Journal of Quantitative Spectroscopy and Radiative Transfer, 110, 1940–1953, 2009.

Peltoniemi, J. I., Kaasalainen, S., Naranen, J., Matikainen, L., and Piironen, J.: Measurement of directional and spectral signatures of light reflectance by snow, IEEE Transactions on Geoscience and Remote Sensing, 43, 2294–2304, 2005.

Peltoniemi, J. I., Suomalainen, J., Hakala, T., Puttonen, E., Näränen, J., Kaasalainen, S., Torppa, J., and Hirschmugl, M.: Reflectance of various snow types: measurements, modelling and potential for snow melt monitoring, in: Light Scattering Reviews 5: Single Light Scattering and Radiative Transfer, edited by Kokhanovsky, A. A., pp. 393–450, Springer Praxis Books, https://doi.org/10.1007/978-3-642-10336-0, 2010.

Peltoniemi, J. I., Gritsevich, M., Hakala, T., Dagsson-Waldhauserová, P., Arnalds, O., Anttila, K., Hannula, H.-R., Kivekäs, N., Lihavainen, H., Meinander, O., Svensson, J., Virkkula, A., and de Leeuw, G.: Soot on snow experiment: bidirectional reflectance factor measurements of contaminated snow, The Cryosphere, 9, 2323–2337, https://doi.org/10.5194/tc-9-2323-2015, 2015.

Pulliainen, J., Aurela, M., Laurila, T., Aalto, T., Takala, M., Salminen, M., Kulmala, M., Barr, A., Heimann, M., Lindroth, A., et al.: Early snowmelt significantly enhances boreal springtime carbon uptake, Proceedings of the National Academy of Sciences, 114, 11 081–11 086, 2017.

Pulliainen, J., Luojus, K., Derksen, C., Mudryk, L., Lemmetyinen, J., Salminen, M., Ikonen, J., Takala, M., Cohen, J., Smolander, T., and Norberg, J.: Patterns and trends of Northern Hemisphere snow mass from 1980 to 2018, Nature, 581, 294–298, https://doi.org/10.1038/s41586-020-2258-0, 2020.

https://doi.org/10.5194/egusphere-2026-2722
Preprint. Discussion started: 21 September 2026

Pulliainen, J., Aurela, M., Aalto, T., Böttcher, K., Cohen, J., Derksen, C., Heimann, M., Helbig, M., Kolari, P., Kontu, A., Krasnova, A., Launiainen, S., Lemmetyinen, J., Lindqvist, H., Lindroth, A., Lohila, A., Luojus, K., Mammarella, I., Markkanen, T., Nevala, E., Noe, S., Peichl, M., Pumpanen, J., Rautiainen, K., Salminen, M., Sonnentag, O., Takala, M., Thum, T., Vesala, T., and Vestin, P.: Increase in gross primary production of boreal forests balanced out by increase in ecosystem respiration, Remote Sensing of Environment, 313, 114 376, https://doi.org/https://doi.org/10.1016/j.rse.2024.114376, 2024.

Rantanen, M., Karpechko, A. Y., Lipponen, A., Nordling, K., Hyvärinen, O., Ruosteenoja, K., Vihma, T., and Laaksonen, A.: The Arctic has warmed nearly four times faster than the globe since 1979, Communications Earth & Environment, 3, 168, 2022.

Roujean, J.-L., Leroy, M., and Deschamps, P.-Y.: A bidirectional reflectance model of the Earth's surface for the correction of remote sensing data, Journal of Geophysical Research: Atmospheres, 97, 20 455–20 468, https://doi.org/https://doi.org/10.1029/92JD01411, 1992.

Spurr, R. and Natraj, V.: A linearized two-stream radiative transfer code for fast approximation of multiple-scatter fields, Journal of Quantitative Spectroscopy and Radiative Transfer, 112, 2630–2637, https://doi.org/https://doi.org/10.1016/j.jqsrt.2011.06.014, 2011.

Spurr, R. J.: A new approach to the retrieval of surface properties from earthshine measurements, Journal of Quantitative Spectroscopy and Radiative Transfer, 83, 15–46, https://doi.org/https://doi.org/10.1016/S0022-4073(02)00283-2, 2004.

Takala, M., Pulliainen, J., Metsämäki, S., and Koskinen, J.: Detection of snowmelt using spaceborne microwave radiometer data in Eurasia from 1979 to 2007, IEEE Trans. Geosci. Remote Sens., 47, 2009.

Taylor, T. E., O'Dell, C. W., Frankenberg, C., Partain, P. T., Cronk, H. Q., Savtchenko, A., Nelson, R. R., Rosenthal, E. J., Chang, A. Y., Fisher, B., Osterman, G. B., Pollock, R. H., Crisp, D., Eldering, A., and Gunson, M. R.: Orbiting Carbon Observatory-2 (OCO-2) cloud screening algorithms: validation against collocated MODIS and CALIOP data, Atmospheric Measurement Techniques, 9, 973–989, https://doi.org/10.5194/amt-9-973-2016, 2016.

Warren, S. G. and Brandt, R. E.: Optical constants of ice from the ultraviolet to the microwave: A revised compilation, Journal of Geophysical Research: Atmospheres, 113, 2008.

Yang, D., Liu, Y., Cai, Z., Chen, X., Yao, L., and Lu, D.: First global carbon dioxide maps produced from TanSat measurements, 2018.

Yang, P., Bi, L., Baum, B., Liou, K.-N., Kattawar, G., and Cole, B.: Spectrally Consistent Scattering, Absorption, and Polarization Properties of Atmospheric Ice Crystals at Wavelengths from 0.2 to 100μm, Journal of Atmospheric Sciences, 70, 330–347, https://doi.org/10.1175/JAS-D-12-039.1, 2013.

Yokota, T., Yoshida, Y., Eguchi, N., Ota, Y., Tanaka, T., Watanabe, H., and Maksyutov, S.: Global concentrations of CO_2 and CH_4 retrieved from GOSAT: First preliminary results, Sola, 5, 160–163, 2009.

Zawada, D., Franssens, G., Loughman, R., Mikkonen, A., Rozanov, A., Emde, C., Bourassa, A., Dueck, S., Lindqvist, H., Ramon, D., Rozanov, V., Dekemper, E., Kyrölä, E., Burrows, J. P., Fussen, D., and Degenstein, D.: Systematic comparison of vectorial spherical radiative transfer models in limb scattering geometry, Atmospheric Measurement Techniques, 14, 3953–3972, https://doi.org/10.5194/amt-14-3953-2021, 2021.